THE FLUID DYNAMICS OF DROPLET IMPACTS ON INCLINED SURFACES WITH APPLICATION TO FORENSIC BLOOD-SPATTER ANALYSIS

A Thesis
Presented to
The Academic Faculty

By

Michael Lockard

In Partial Fulfillment
Of the Requirements for the Degree
Master of Science in Mechanical Engineering

Georgia Institute of Technology

August 2015

THE FLUID DYNAMICS OF DROPLET IMPACTS ON INCLINED SURFACES WITH APPLICATION TO FORENSIC BLOOD-SPATTER ANALYSIS

Approved by:

Dr. G. Paul Neitzel
School of Mechanical Engineering
Georgia Institute of Technology

Dr. Marc K. Smith
School of Mechanical Engineering
Georgia Institute of Technology

Dr. Srinivas Garimella
School of Mechanical Engineering
Georgia Institute of Technology

Date Approved: June 23rd, 2015

Acknowledgments

Table of Contents

List of Tables

List of Figures

vii

List of Symbols and Abbreviations

V	Velocity
D	diameter
θ	impact angle
ρ	density
μ	dynamic viscosity
σ	surface tension
ε	surface roughness
Re	Reynolds Number
We	Weber Number
La	Laplace Number
e	eccentricity
D_0	impact diameter
D_s	stain diameter
V_0	impact velocity
N	number of spines
Δz	distance between lasers
t_{p-p}	peak-to-peak time
SF	spread factor
A_f	final area
A_D	cross-sectional area of a drop

Summary

Bloodstain pattern analysis is used in the investigation of a crime scene to infer the impact velocity and size of an impacting droplet and from these, the droplet's point and cause of origin. The final pattern is the result of complex fluid dynamic processes involved in the impact and spreading of a blood drop on a surface with variable surface properties such as wettability and porosity. An experiment has been designed to study these processes and the resulting patterns for the case of a single Newtonian droplet impacting an inclined surface with variable roughness and wetting properties. An experimental apparatus, including a droplet generator, has been designed to produce droplets on-demand, and that impact an interchangeable surface. In addition, a blood-simulant liquid has been developed as a replacement for performing tests with real blood. With this apparatus and blood simulant, fluid dynamics concepts, such as contact line motion and wetting behavior are examined in the context of parameters of interest to the forensics community. These include eccentricity, spread factor and the number of spines formed on impact. The effect of varying dimensionless parameters including Reynolds number, Weber number and Laplace number, the angle of impact and surface properties is examined. Correlations are developed for predicting conditions at the point of impact from those observed later, as would be available to a forensics examiner, and the accuracy of the predictions developed in this thesis are evaluated.

Chapter 1 - Introduction

Crime scene reconstruction is the discipline of determining events surrounding a crime based on scientific methods, deductive reasoning, physical evidence and their interdependencies. Various techniques have been used for this reconstruction. Among the most commonly used processes are DNA evaluation, fingerprint identification, and the focus of this thesis, blood-spatter analysis. Blood-spatter analysis uses residual bloodstains left at the scene of a crime to determine the point of origin of a particular stain and the type of trauma that led to the bloodletting (e.g., gunshot, blunt force, sharp object, etc.) [1]. The determination of these factors assists crime-scene analysts in their efforts to establish the sequence of events that occurred during the crime. It is known that the size and shape of a bloodstain are caused by conditions at the point and time of impact [2]. Stain size is quantitatively described as the area of the stain's elliptical shape, whereas shape is quantified by the stain's eccentricity as well as the number of spines and satellite drops around the stain contour [2] [3] [4]. The area of a stain is measured by fitting an ellipse to the stain outline and measuring the major and minor diameters, denoted by L and W respectively in Figure 1 [5].
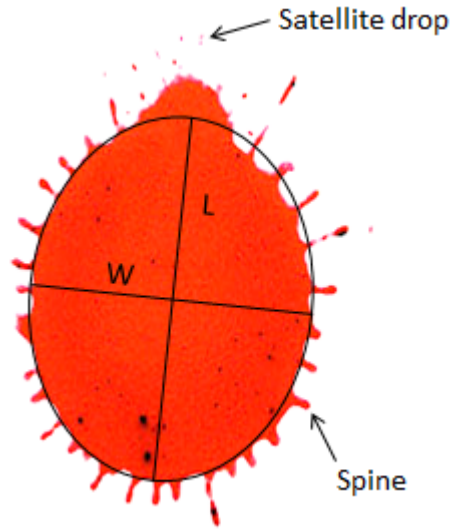
Figure 1. Illustration of primary stain features [6].

Eccentricity (*e*) is a relationship between these diameters.

$$e = \frac{L}{W} \tag{1.1}$$

A spine is a disruption in the periphery of a stain whereas a satellite is a drop that has completely separated from the main body.

Within this general framework, where stain eccentricity, size, and shape, are used to determine impact conditions, a multitude of specific models and tools are used [7] [1]. The use of specific correlations, strategies, software, etc., is dependent on the resources available to an examiner, which are impacted by where and for whom the examiner works. One very popular, long-standing technique is called stringing [2]. This method

uses the eccentricity of a drop to determine its direction of origin by way of equation 1.2, where θ is the impact angle.

$$\theta = \arccos(1/e) \qquad (1.2)$$

Balthazard, Piedelivre, Desoille and DeRobert proposed this relationship in 1939, based on their experimental work, and it has become the predominant correlation in forensics analysis [2]. Using this relationship, a ray is drawn in a straight line from the stain in the direction of θ. A nexus, or region of convergence, is then determined, by considering rays from a large number of stains. The point of origin is presumed to be the point of intersection of many rays. Additionally under this method, the speed of the drop is determined by the size of the stain and the assumption that the volume of the blood drop was "normal" [2], where a "normal" drop is defined as one containing 0.05 mL of blood [2]. This technique assumes that all stains are created by drops of equal volume.

Recently, more refined methods have been developed in an effort to reduce sources of error. Ballistics software has allowed for a more rigorous application of physics in determining droplet flight paths [1]. Using these tools, gravity, drag and other forces acting on a drop in flight may be taken into account. Correlations have also been developed that relate the number of spines to droplet speed at impact [3] [4]. With these developments, the assumption of a drop of "normal" volume is no longer required. Although these methods represent significant improvements over previous methods, they are still limited. A correlation is only valid for impacts within a certain range of impact conditions and for impacts on a certain material. Surface properties such as roughness, compliance, and porosity affect spreading behavior and can either inhibit or

promote spine and satellite formation [8] [9]. Thus, a more complete examination of the physics of droplet impacts may improve current blood stain examination techniques and lead to less ambiguity in the events surrounding crime-scene blood-spatter analysis.

It is helpful in the discussion of droplet impact behavior to separate the droplet impact process into four stages: pre-impact, spreading, retraction, and progression towards a steady-state; Figure 2 illustrates the first three stages. Note that all droplet impact images in this thesis are shown for impacts on inclined surfaces. The surface slants downwards from left to right in every image, resulting in greater spread in this direction.
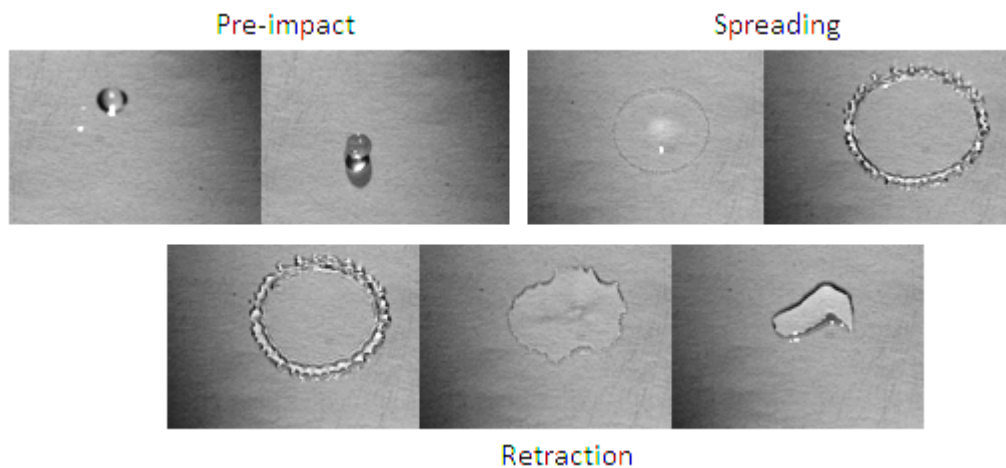
Figure 2. Illustration of droplet impact stages. This impact is for a 2.4mm diameter water drop, traveling at 3.46m/s, impacting glass at an angle of 20°. For each group of images, time increases from left to right.

Pre-impact is the time after droplet generation but preceding the collision of the drop with the surface. While the droplet is in free-fall, gravity accelerates the drop downward, the surrounding air exerts a drag force, and the droplet may experience oscillation due to its

4

method of origination and/or aerodynamic forces. Impact signals the end of this stage and the beginning of the spreading stage. Spreading begins on impact and ends when the wetted area of the substrate reaches a maximum. At this point in the impact process, retraction begins. Retraction is caused by surface tension in the liquid pulling the lamella back into itself. A lamella is a thin rim on the outside edge of a drop that frames it as it spreads, as illustrated in Figure 3.
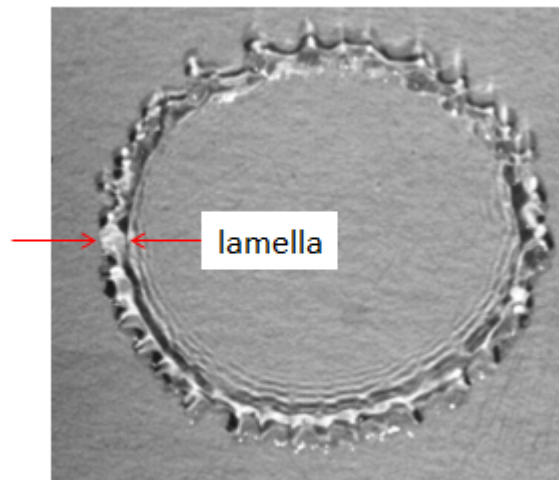
Figure 3. Illustration of a lamella. Notice how light is reflected differently in the layer on the edge of the drop. This is the lamella.

The cohesive, intermolecular, forces within a droplet must overcome the adhesive forces between the droplet and the surface for this to occur. Compared with water, blood has a smaller surface tension. Whereas water tends to retract, blood will remain in a small pool. Figure 4 shows an impact where there is noticeable retraction versus an impact where retraction is imperceptible.
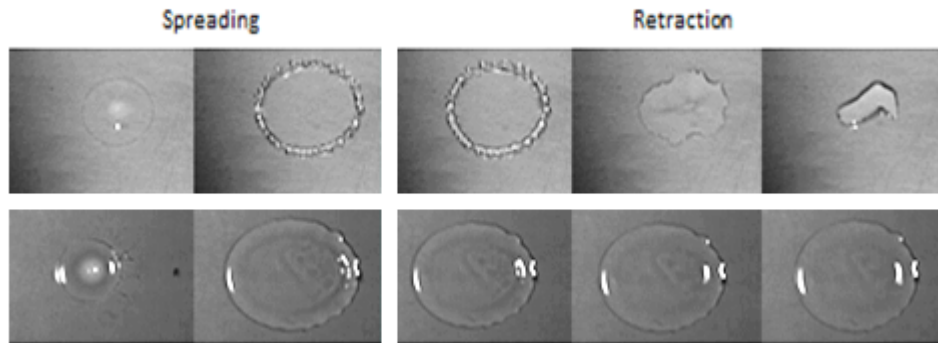
Figure 4. Retraction stage illustration. The top images show an impact progression for water. The bottom images show an impact progression for a blood simulant liquid.

The final stage exhibits a progression toward a steady-state shape. During this stage, ambient conditions and particular solid-surface properties play greater roles than in previous stages. For example, liquid can be wicked into the material being impacted, it may begin to flow due to its own weight and drying may inhibit flow.

When studying droplet impacts in the context of forensics, the spreading stage is of the greatest importance. A stain is, by definition, "a discoloration produced by foreign matter having penetrated into or chemically reacted with a material" [10] and in the case of blood stains, blood residue bonds with the substrate. Blood residue left behind on a surface can be observed either visually or with the help of chemicals such as luminol. Luminol exhibits chemiluminescence when it reacts with an oxidizing agent and is the predominant chemical used in blood-spatter analysis [11] [12]. What luminol illuminates and what the eye observes in these images, is the result of the spreading stage of a droplet impact. The spreading stage is also the period when behavior is most affected by the impacting droplet properties. Retraction is minimal for blood due to its relatively low surface tension, and steady-state blood drops are affected by ambient conditions such

as temperature and humidity as much as by the droplet properties at impact. Additionally, wicking and drying behavior are relevant to steady-state analysis while these effects are much less prevalent during the spreading phase.

From the perspective of fluid dynamics, droplet impacts can be studied by examining wetting behavior and contact line dynamics. Wetting is the ability of a liquid to adhere to a solid surface. Often, the wettability of a surface is quantified by the contact angle α, shown in **Figure 5**, measured through the liquid, of a liquid/vapor interface at the three-phase line on a solid surface. As the contact angle decreases, the wettability of the surface is said to increase.

Profile view
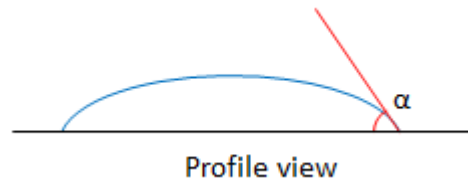
Figure 5. Contact angle illustration.

Wettability, contact line and contact angle can be studied in terms of impact parameters such as droplet velocity (V), diameter (*D)* and impact angle (θ), fluid properties such as density (ρ), viscosity (μ) and surface tension (σ), and surface properties such as average roughness (ε), hardness, wettability, and porosity. Impact and fluid properties can be reduced in number through dimensional analysis, leading to the dimensionless Reynolds number *Re*, Weber number *We*, and Laplace number *La*, only two of which are independent:

$$Re = \frac{\rho V D}{\mu} \qquad (1.3)$$

$$We = \frac{\rho V^2 D}{\sigma} \qquad (1.4)$$

$$La = \frac{\rho \sigma D}{\mu^2} = \frac{Re^2}{We} \qquad (1.5)$$

These dimensionless parameters are important in the present problem because they indicate relative magnitudes of forces at play during impact. Re represents the ratio of inertial to viscous forces, We is the ratio of inertial to surface-tension forces and La is a ratio between surface tension and momentum transport within a fluid. In order to study droplet impacts systematically, these parameters must be varied and the resulting stain patterns, including the time-dependent spreading behavior, must be observed. In forensics these dimensionless parameters fall into the following ranges, based on the properties of blood and the size and speed of droplets seen in forensics:

$100 < Re < 25,000$, $5 < We < 180,000$, $3,000 < La < 25,000$ [13].

On the subject of the fluid dynamics of blood-spatter analysis, a number of previous studies were important in the development of this thesis. Adam [4] experimentally validated relationships between droplet size and velocity and the resulting stain size and the number of spines. Adam used stored human blood and focused specifically on droplet impacts on paper. For the range of droplet sizes and speeds tested, he concluded that there was strong dependence of the number of spines and stain size on

the impact speed. The majority of his work was focused on perpendicular impacts, but

he performed a limited amount of work on inclined surfaces. He posited a relationship

between the number of spines, the impact angle and *We* of the form shown in equation

(5).

$$N = We^{\frac{1}{2}} \sin(\theta)^{\frac{7}{2}} \tag{1.6}$$

Carroll [14] also conducted droplet-impact research and it is her method of droplet

generation that formed the starting point for the generator design outlined later. Carroll

used a glycerin-water mixture and similarly concluded that number of spines was

dependent on the impact velocity. She also found that eccentricity was wildly

unpredictable when comparing results obtained for different impact angles and

materials. These results run counter to many standard practices in the forensics

community and bear further investigation.

Finally, Hulse-Smith and Illes [3] used human blood to experiment with stain patterns on

paper, wood and drywall for perpendicular impacts. Using their experimental results they

developed correlations between droplet impact size D_0, speed V_0, and the number of

spines produced in the corresponding stain. An additional correlation between the

diameter of the stain, D_s, and the impact diameter was developed, since two equations

are necessary to solve for two independent parameters. Using these two correlations,

the incoming diameter and velocity were calculated from the number of spines and the

stain diameter. The correlations developed in this paper neglected liquid properties,

arguing that since liquid properties are the same for all impacts, using dimensional

correlations was more practical. These correlations include only variables that were

measured and those that need to be calculated.

$$N = 146 D_0 V_o^2 + 12.8 \qquad\qquad (1.7)$$

$$\frac{D_s}{D_0} = 13.8 \sqrt[3]{D_0 V_0} \qquad\qquad (1.8)$$

Although each of these sources provides invaluable insight into various aspects of droplet behavior, many questions remain. To this end, the purpose of the research presented in this thesis is to investigate the fluid dynamics of a drop impacting an inclined surface. The effects of surface properties and impacting conditions (drop size, speed, etc.) are examined. The resulting stain and the spreading behavior of a drop under various conditions are of particular interest. The study of this behavior will assist forensic examiners in their attempts to reconstruct crime-scene events.

Chapter 2 - Methods

The work to be described in this thesis is comprised of a set of laboratory experiments, where single droplets are ejected onto a target surface. The spreading behavior of each individual droplet is then studied through use of high-speed photography. Toward this end, an experimental apparatus is needed that can fulfill three primary functions: first, it must reliably produce droplets; second, it must be capable of varying the desired parameters of interest; and finally, it must permit the measurement of relevant data. The final experimental setup, shown in Figure 6, is composed of the droplet generator; the test frame; and the target assembly. The droplet generator is used to produce droplets on demand. The material onto which droplets fall is placed on the target assembly. This subsystem also allows for the measurement and variation of parameters. The lasers and photodiodes depicted in Figure 6 are used to measure a droplet's speed. The generator is mounted on a platform that slides vertically between two rails. This allows for variation of the height a droplet falls. It also serves as a support structure for the entire assembly. Each sub system is described in greater detail in the following subsections.
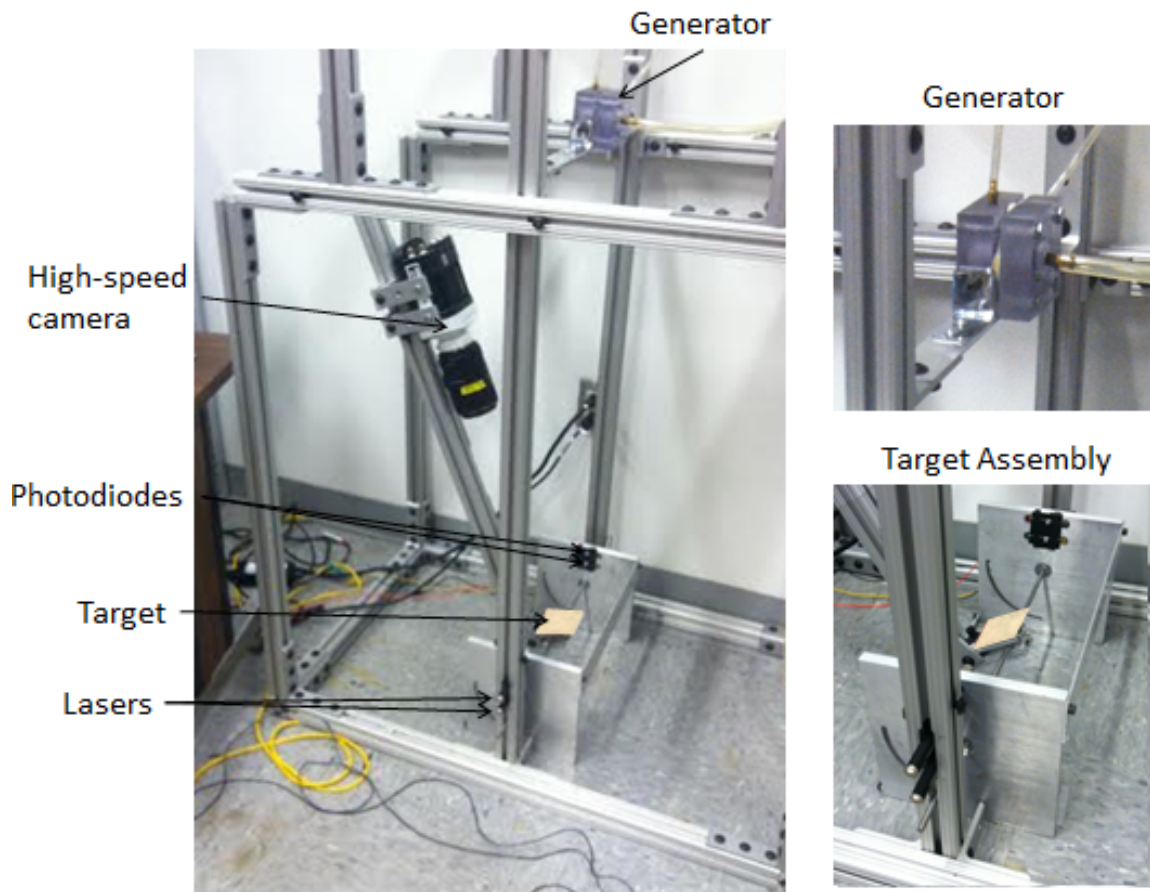
Figure 6. Experimental setup.

2.1 The Droplet Generator

The droplet generator is used to physically produce single droplets-on-demand of various sizes. The system operates on the principle that liquids are incompressible. Liquid is allowed to flow into a chamber; after, the chamber is filled the inlet and outlet are sealed off. By deflecting a membrane into the liquid supply, liquid is forced out of the chamber through an orifice. In order to describe droplet generation in more detail, the droplet generator subsystem can be further divided into three subsystems: the air section; the liquid section; and the control circuit.

The air section is composed of a compressed air supply and a pressure regulator. Air is pulsed into the generator deflecting a flexible membrane. Changing the duration and magnitude of the pressure pulse changes the deflection profile and, ultimately, the size and speed of the ejected droplet. The magnitude of the pressure pulse is controlled with the pressure regulator and its duration with a solenoid valve. The purpose of the control circuit is to actuate this solenoid valve. A LabVIEW program was written to precisely control a relay that acts as the breaker for the solenoid valve circuit. A National Instruments DAQ acts as the computer-relay interface.

The liquid section is composed of a liquid supply, a liquid reservoir, and the droplet generator. Two ball valves control the flow of liquid through the generator. Figure 7 shows how these three subsystems interface and how information, air and liquid flow through the system. The droplet generator, shown without detail in Figure 7, is the key component of the system from a design standpoint.
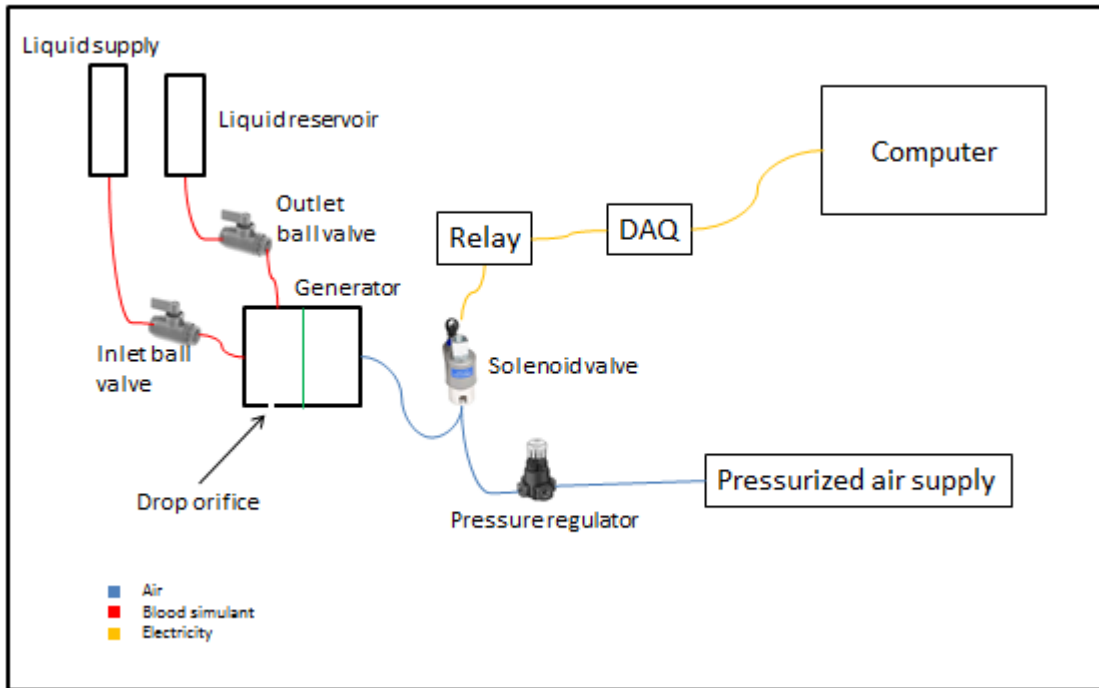
Figure 7. System Components and their Interactions. Separate systems are identified by different colors.

The starting point for the design of the droplet generator was one taken from the previous work of Carroll [7], but several important design changes were made, with the final design shown in Figure 8. The first significant change is the orientation of the generator. The direction of membrane deflection (i.e., whether downwards, sideways, etc.) is not important. Thus, the membrane and air chamber were moved to the side of the liquid chamber, rather than above it. Additionally, a cone was fashioned into the top of the liquid chamber. Air bubbles travel around the side of the cylindrical chamber and upon reaching the cone, are funneled up through the air vent. Changing the orientation also allowed for the addition of a large, threaded hole to accommodate threaded orifices of different sizes. This was not possible in the previous model, due to lack of material in

the thin plastic sheet used as a liquid chamber bottom. With this addition, the orifice could then be used to vary the size of a drop being produced. Another important modification was changing the membrane mounting method. Instead of mounting a single membrane clamping plate to the inside of the liquid chamber, two membrane clamping plates secured the membrane and the entire apparatus was clamped together via bolts. This revised clamping design allows for much greater and more precise pre-tensioning of the membrane and makes mounting the membrane easier. Greater membrane tension increased the ejection speed and decreased the incidence of satellite drops.

Operation of the generator begins with filling the liquid chamber. To do this, the orifice was plugged with a rubber stopper and the inlet and outlet ball valves were opened. Liquid was allowed to flow until all air bubbles were evacuated from the chamber. At this time, the outlet ball valve was closed, followed by the inlet valve. The orifice plug was then removed. In the development of this system there was concern over air remaining in the channel between the liquid chamber and the orifice. After unplugging the orifice, a small amount of liquid is seen to drip from the opening, dispelling these concerns. After the initial dripping, the liquid is completely stagnant until a droplet-producing air pulse is applied. Figure 9 roughly illustrates operation of the modified generator.
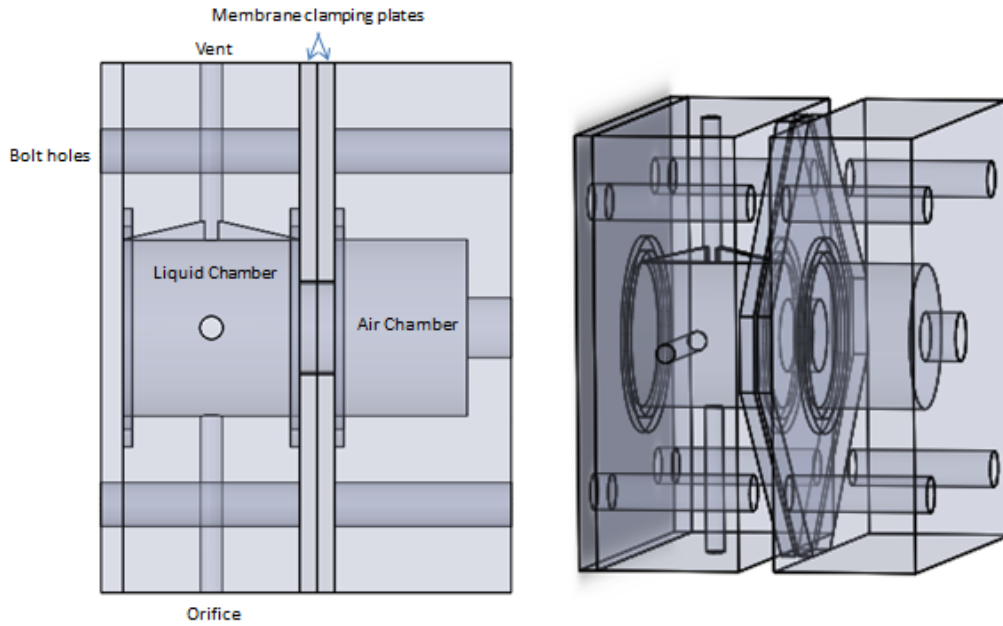
Figure 8. Final droplet generator design. This image includes the air and liquid cambers, the clamping plates and the liquid chamber bottom piece. Also shown are the bolt holes and the O-ring groves.
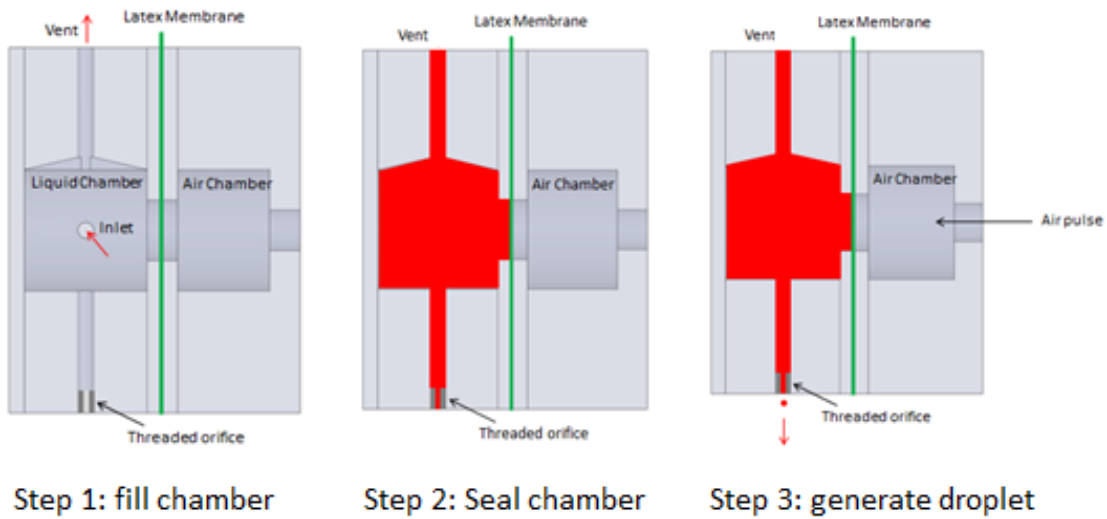
Figure 9. Droplet generator operation. Step 1 – fill the chamber with liquid. Step 2 – close off the inlet and vent. Step 3 – pulse air into the air chamber to deflect the membrane and produce a drop.

16

In addition to producing drops of varying size, the ability to vary speed is also desired. A decision was made to use gravity to accelerate a drop instead of accelerating either the generator and/or the target toward one another. Accelerating the target toward the drop would also allow for large impact speeds, but aerodynamic effects due to the moving platform might interfere with the drop in flight, causing unpredictable behavior. To utilize gravitational acceleration, the droplet generator was mounted on a sliding platform between a pair of rails, allowing for an adjustable drop height. A drop accelerates over the fall distance to a desired speed with terminal velocity providing a limitation on velocity variability. A drop height of 2.5m was determined to be sufficient to reach a near-terminal speed. Prefabricated T-slot structural aluminum rails were used to fabricate the apparatus. Figure 10 shows how they were assembled to provide the given function. An additional support frame was constructed around the two main rails and is not shown in the graphic.
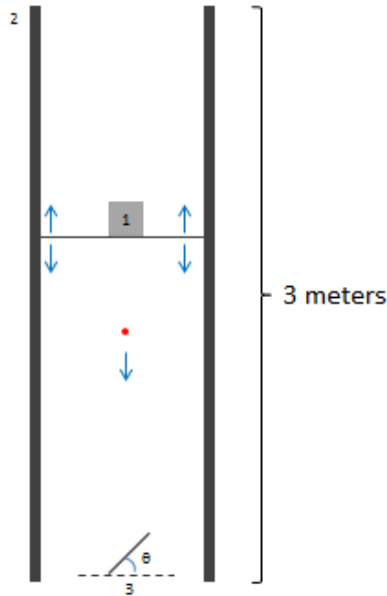
Figure 10. Rail system layout. The numbers in the figure show how the generator (1) was placed on a sliding platform between rails (2), while always being directly above the target (3).

Using the generator described in the previous section, droplets can be reliably and predictably produced, without satellite drop formation, with diameters ranging from 2mm to 5mm. The use of rails allows for acceleration of these drops up to speeds of 5 m/s. To place this into forensics context, this would correspond to drops created via cutting or blunt force. Droplets resulting from a gunshot wound are typically smaller and move at much greater speeds. For drops in the size range described, the speeds resulting from gravitational acceleration represent a near-terminal speed. We can compare these operational parameters to work done by Carroll [14] and Adam [4]. Carroll was able to produce droplets between 1.5 and 4.5 mm in diameter capable of speeds between 1.7 and 2.1 m/s. It is important to note that droplet size was the determining factor in speed. Since weight changes on the order of diameter cubed and drag varies on the order of

18

diameter squared (drag also changes on the order of velocity squared), smaller drops arrive at the target at slower speeds. The rail system described above has the advantage of producing drops of much greater speeds, which can be adjusted without changing the size of the droplet produced. Adam used dripping to produce drops of 3.28, 4.21 and 5.15 mm in diameter. One of the great advantages of using a droplet generator over dripping is the ability to produce drops of smaller sizes and to vary the size of a drop without changing the orifice used to produce them. Dripping occurs when the weight of the drop overcomes the force of adhesion between itself and the orifice material. By using the droplet generator described in the preceding sections, this limitation is overcome via a pressure pulse. Additionally, the magnitude and duration of the pressure pulse can be used to vary a droplet's size within a small range. This allows for greater flexibility when different sized droplets are desirable.

2.2 The Target Assembly

After a drop is produced by the generator and falls a distance that is controlled by the rail system, it collides with a surface mounted on a target plane. The target assembly, onto which targets are placed, allows for measurement of the parameters of interest and allows for the target to be interchangeable. In this way, impacts on different materials can be studied. The target assembly consists of a rotating shaft, a camera arm and a frame. The camera arm mounts rigidly onto the rotating shaft, which slides into bearings on either side of the frame. This assembly, shown in Figure 11, ensures that the camera is always oriented perpendicularly to the target, which is necessary when studying spreading behavior. An oblique viewpoint would distort measurements of drop characteristics.

19
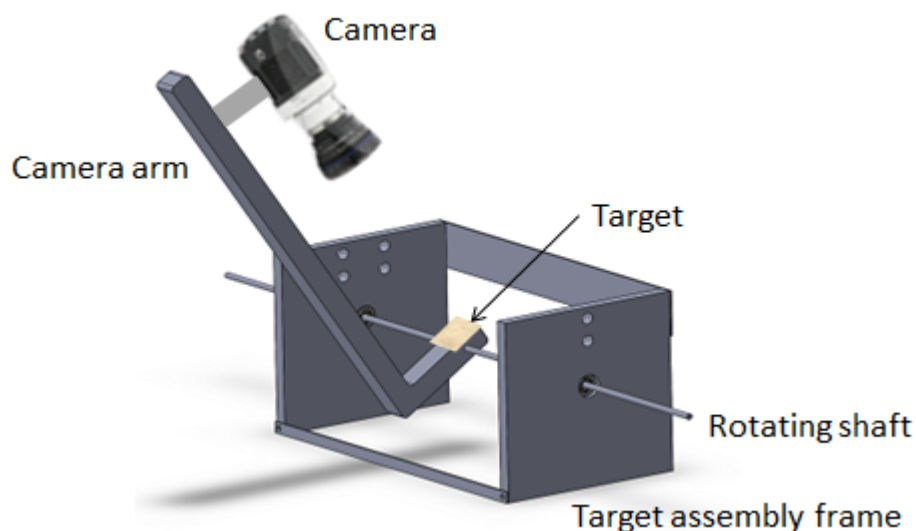
Figure 11. Target assembly.

Since high-speed video is employed for these experiments, one might be tempted to extract a droplet diameter from a video frame. However, droplet deformation due to aerodynamic effects and/or persistent oscillation makes this difficult. Since the high-speed camera is mounted in such a way that it is always perpendicular to the impact surface, information is only available within a single plane. This is desirable for studying spreading behavior, but not for studying a droplet in flight. A droplet in flight deforms in more directions than the single plane for which we have information. Therefore, a more reliable method for determining droplet size is to measure its mass. By measuring the mass of the target before and after a drop impact, the mass of the impacting drop is determined to within four ten-thousandths of a gram. A Mettler AE160 analytical balance was used to make these mass measurements. Mass measurements were taken within ten seconds of impact. Over this time period, evaporation was experimentally determined to be insignificant. For each material, the weight of the target and a liquid

drop was recorded over a minute. At the end of the minute the weight was within four

ten-thousandths of a gram, in each case.

In order to measure droplet speed, a method was designed using two laser/photodiode

pairs. Each laser illuminates a photodiode located horizontally opposite it. Each beam

produces a constant current from the photodiode. The two laser/photodiode pairs are

oriented vertically and separated by a distance Δz, shown in Figure 12, so that the

beams cross the path of a falling droplet. As a liquid drop passes through each beam

the current produced shows a sharp spike, shown in Figure 13, which is measurable via

a LabVIEW data acquisition program. Using this program to determine the time, $t_{p\text{-}p}$,

between blips, given the known Δz, a speed, V, can be computed according to equation

(2.1).

$$V = \frac{\Delta z}{t_{p-p}} \tag{2.1}$$

Figure 12 illustrates how a drop blocks each laser as it passes through the beams, and

Figure 13 shows an example of the current vs time produced by the passage of a

droplet.
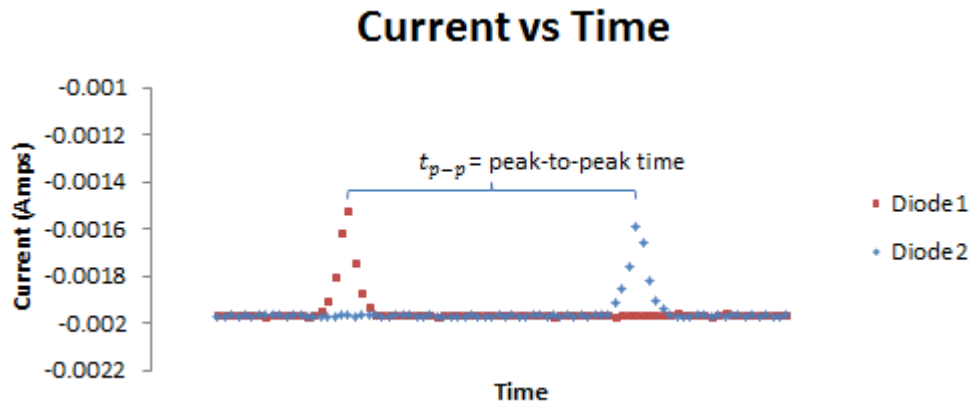
Figure 13. Speed calculation from the photodiode data.

The other necessary parameter is the impact angle. To control this precisely, the impact platform was placed on a rotating shaft. The shaft passes through the target assembly, shown in Figure 11, and through the main rails of the rail system. In doing so, the center of the target assembly was always centered under the droplet generator. Also note in Figure 11 the two holes on one side of the mount and four holes in a rectangular pattern on the other. These are for integration of the laser-photodiode system described above. A laser is placed in each of the two holes on the right, while a photodiode is placed in the center, horizontally of each pair of holes on the left. The holes on the left are used for wiring the photodiodes to a National Instruments USB-6008 DAQ device. The L shape of the target assembly is necessary for mounting a camera such that the viewing direction is orthogonal to the target and the center of the frame is the location of impact. A

Phantom Miro M120 high-speed camera is used to record droplet impacts and analyze spreading behavior.

2.3 Blood Simulant

With a method in-hand to produce droplets reliably, attention turned to developing a blood simulant to model the properties of blood during impact conditions. For Reynolds numbers (1000 < Re < 6000) and droplet sizes (scaled by the length scales of blood's particulate components) lying within the capabilities of this apparatus blood can be modeled as a Newtonian fluid. In addition, on the time scale of a droplet impact, the effects of drying and capillary action (i.e., "wicking") were determined to be negligible. Droplet spreading occurs on the order of milliseconds, much less than the amount of time needed for wicking to occur, which is on the order of seconds. High-speed photography was used to verify this assumption. Under these conditions the physical properties of interest are the viscosity and surface tension. According to Adam [1], the kinematic viscosity of blood is 4.15 cSt and its surface tension is 62 mN/m. By matching both the viscosity and surface tension of actual blood, one is able to easily achieve dynamic similarity between blood-simulant experiments and actual practice.

Since blood can be modeled as a Newtonian liquid under the test conditions applicable to this experiment, a simple and easy-to-use blood simulant liquid was prepared: a mixture of water, glycerin and alcohol. Using tap water as the base liquid (with nominal values of 1 cSt and 79 mN/m for viscosity and surface tension, respectively), the viscosity needed to be increased and the surface tension needed to be decreased for

the simulant liquid to have the appropriate properties. Glycerin was readily obtainable, is miscible with water, and has the desired effect of increasing viscosity. Adding isopropyl alcohol was determined to be an economic and effective means of reducing the surface tension. Additionally, the small quantities of alcohol used did not significantly affect the viscosity. At ambient conditions under which experiments were later performed, calibration curves were developed to determine the appropriate amounts of each liquid needed to hit the target physical properties. Due to the temperature-dependent nature of viscosity of water-glycerin mixtures, ambient conditions were carefully monitored to ensure that test conditions were constant, and liquid properties were invariant. Viscosity was measured using a Cannon-Fenske Routine viscometer and the surface tension was measured by the pendant drop method [15]. The simulant liquid was prepared and tested before each experimental run to verify that properties conformed to the specifications.
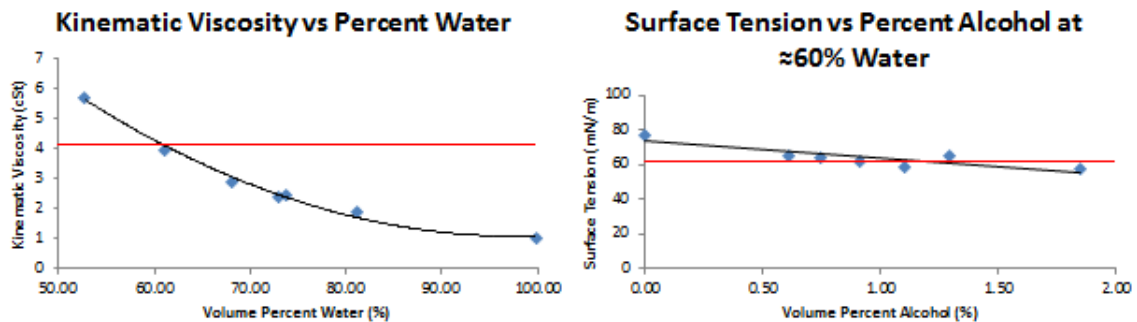
Figure 14. Blood simulant calibration curves. The red line indicates the desired properties of blood.

Several other simulant liquids were also researched. The first was the use of water with the addition of a surfactant. This could have been used instead of alcohol to lower

surface tension, but due to price, was dismissed. Second, a number of commercially available products were considered. Products such as TrueClot® and NoStainSim claim to match the properties of blood, but were dismissed, again, due to cost considerations. A variety of studies including that by Hulse-Smith [3] used actual human blood. Due to the difficulties inherent in the use of biological samples (including the approval process), acquiring samples, storage and sample degradation, this option, too, was discarded. Finally, Michielsen et al. [16] used a synthetic blood simulant based on ASTM standards. Although this was a viable option, confirming that the simulant properties matched those of real blood was only possible after purchasing the standard. Therefore, due to cost considerations, and an existing and functional simulant, this, too, became a secondary option.

Chapter 3 - Experimental Procedure

Using the setup and simulant liquid described in the preceding sections, data were taken for various droplet and impact-surface properties. The properties that were directly adjustable include the drop diameter and speed (corresponding to changes in *Re*, *We* and *La*) the angle of impact and the material involved. In the analysis of the data collected, *We* has been excluded from the discussion due to the similar trends seen for both *Re* and *We*. Different results may be evident over a larger range of *Re* and *We*, but not for the range of these parameters tested in this experiment.

Three different materials were used in order to evaluate the effects of surface roughness and absorptivity: glass, a glazed semi-rough ceramic tile, and construction paper. For the purposes of this study, roughness and absorptivity were the primary surface properties of interest. Table 1 lists all of the properties that were varied and the ranges through which they were varied. Shown are both the specific properties that were adjusted and the dimensionless values required for analysis. Roughness values were obtained using a profilometer available in the Georgia Institute of Technology School of Mechanical Engineering machine shop. Absorptivity values were taken by measuring the ratio, by volume, of water to material after it had been allowed to soak. A more detailed description of the method is detailed in reference [17]. It is important to note the anisotropic nature of the roughness of paper. The lower value is the roughness in the direction of flow, while the higher value is the roughness across the surface. When experimenting with paper, each sheet was always oriented in the same direction, with greater roughness in the transverse direction.

Table 1. Parameter ranges and materials used for these experiments.

Property	Range
Diameter (mm)	2-5
Velocity (m/s)	1-5
Reynolds Number	1000-5500
Weber Number	200-2000
Laplace Number	4000-15000
Impact Angle (deg.)	20-60
Impact Surface	Glass, Tile, Paper

Table 2. Roughness and absorptivity values for the three materials used. ε refers to the arithmetic average of a surface profile from its centerline and absorptivity refers to the percent, by volume, of water to the listed material after soaking. The two values shown for the roughness of paper correspond to the roughness in the longitudinal and transverse directions respectively.

	Glass	Tile	Paper
Roughness (ε)	0.002	0.048	0.224 / 0.292
Absorptivity (%)	<<1	<1	14.8

The procedure for collecting data was the following. First, the height of the droplet generator was fixed, fixing the droplet speed, and an orifice was chosen, limiting the range of droplet diameters capable of being produced. For each material, the angle was then varied between 20° and 60° in increments of 10°. Next, either the drop height or the orifice was varied, changing *Re*, *We,* and/or *La*. Four different orifices were used including 0.063 in, 0.1 in, 0.125 in and 0.2 in. When placing a material onto the target,

care was taken to ensure that each surface was as similar as possible to others used in similar test runs. For paper, this meant that the same orientation was used for each test run. For glass and tile, this involved rinsing the surface with water, drying it, and then using a blowtorch to fire-clean it. Fire-cleaning was implemented to remove as many dust and paper particles as possible. At each angle, speed, size and material, at least two data points were collected to validate the behavior. For each individual test a video was collected. Videos were taken from just prior to impact until the drop had spread out and retracted, typically on the order of half of a second. Information was gathered from these video records, including the major and minor diameters of an ellipse fit to the drop contour, as well as the number of spines. The major and minor diameters were measured from the outside edge of the droplet lamella. Figure 15 shows how an ellipse is fit to a droplet contour when it is not perfectly elliptical.
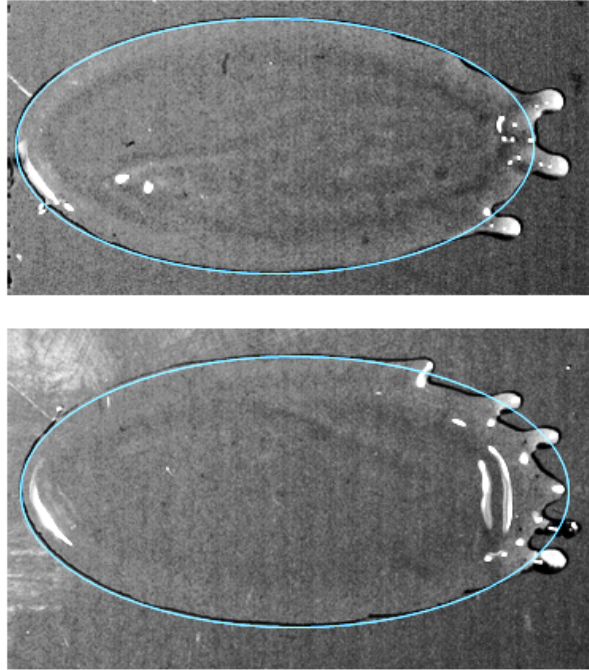
Figure 15. Illustration of an ellipse fit to non-elliptical droplets. Both images are for impacts on glass at an angle of 50°

After each drop was fit with an ellipse, the number of pixels along the major and minor diameters was determined. A scale was also included in each image, allowing a conversion from the number of pixels to a distance.
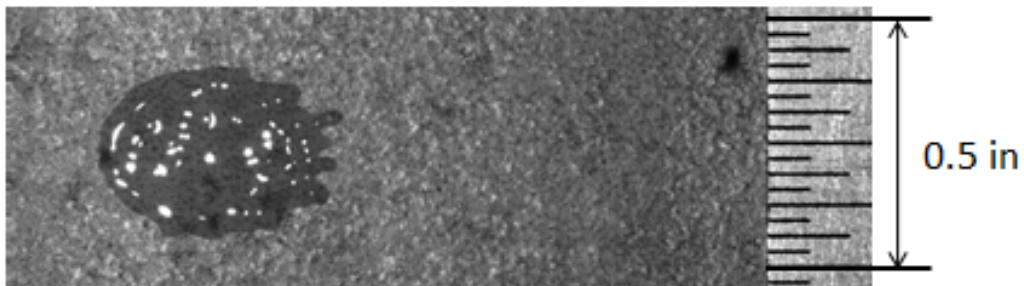
Figure 16. Droplet next to a scale. This image shows a drop impacting a tile surface at an angle of 30°.

Chapter 4 - Results

The product of the experimental methods and procedures outlined previously is a study of three parameters of interest: eccentricity, spread factor and the number of spines. These properties are examined against the impact angle, *Re*, the impacted material and *La*. Spread factor (SF) is the ratio between the cross-sectional area of an incoming droplet and the area of the resulting stain.

$$SF = \frac{A_f}{A_D} \tag{4.1}$$

A_f and A_D are the area of the final shape and the cross-sectional area of the drop, respectively, as shown in Figure 17.
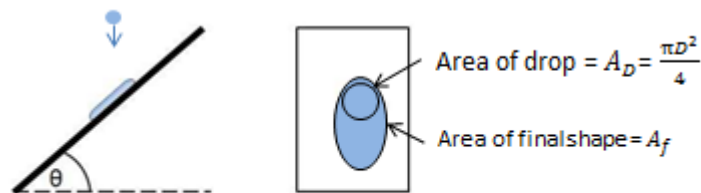
Figure 17. Spread factor illustration

For each parameter, observed trends are explained and correlations are developed. Once eccentricity, spread factor and the number of spines are examined individually, the method for using the developed correlations in forensics analysis is explained. Also, the conditions necessary for applying each correlation are described.

4.1 Eccentricity

Recall that eccentricity is the ratio between the major and minor diameters of an ellipse fit to a blood stain. In forensics, the common practice is to obtain the impact angle from the measured eccentricity using the simple relationship.

$$\theta = \arccos(\frac{1}{e}) \qquad (4.2)$$

One objective of this chapter is to determine the accuracy of this correlation and offer a more complete picture if this relationship is found to diverge from experimental results. This discussion begins with an examination of eccentricity versus Re, for each material in Figure 18, Figure 19, and Figure 20. In these plots, as well as others presented throughout the remainder of this thesis, the measurement uncertainty of a single data point is between 2% and 5% of the measured value; however, there is significant variation over droplets produced under similar conditions, especially for impacts on paper. In order to quantify this effect, a series of 15 data points was collected on each surface at an angle of 40° and with Re = 5300. The results are shown in Table 3.

Table 3. Tabulated variability of eccentricity.

	Glass	Tile	Paper
Average Eccentricity	1.41	1.42	1.44
Standard deviation of Eccentricity	0.03	0.03	0.09

Table 3 illustrates that there is variability even when the droplet size and speed are kept constant. Paper shows significant variation, where eccentricities of 1.35 - 1.53 represent

one standard deviation in either direction. Glass and tile show less, but still a noteworthy amount of, variability. Two hypotheses for this variability are presented here. The first is the difference between microscopic and macroscopic roughness. This is particularly relevant for impacts on paper and to a lesser extent for impacts on tile. Although the average roughness over the distance measured by a profilometer does not change based on location for any of the surfaces tested, this average value is probably not obtained in a uniform fashion. In other words, roughness may differ over very small distances, but the average roughness over the entire domain can remain constant. The second is that an oscillating drop may impact a surface at different phases within an oscillation period. For a smooth surface, such as glass, droplet oscillations are the most likely cause of the spread seen in the data.
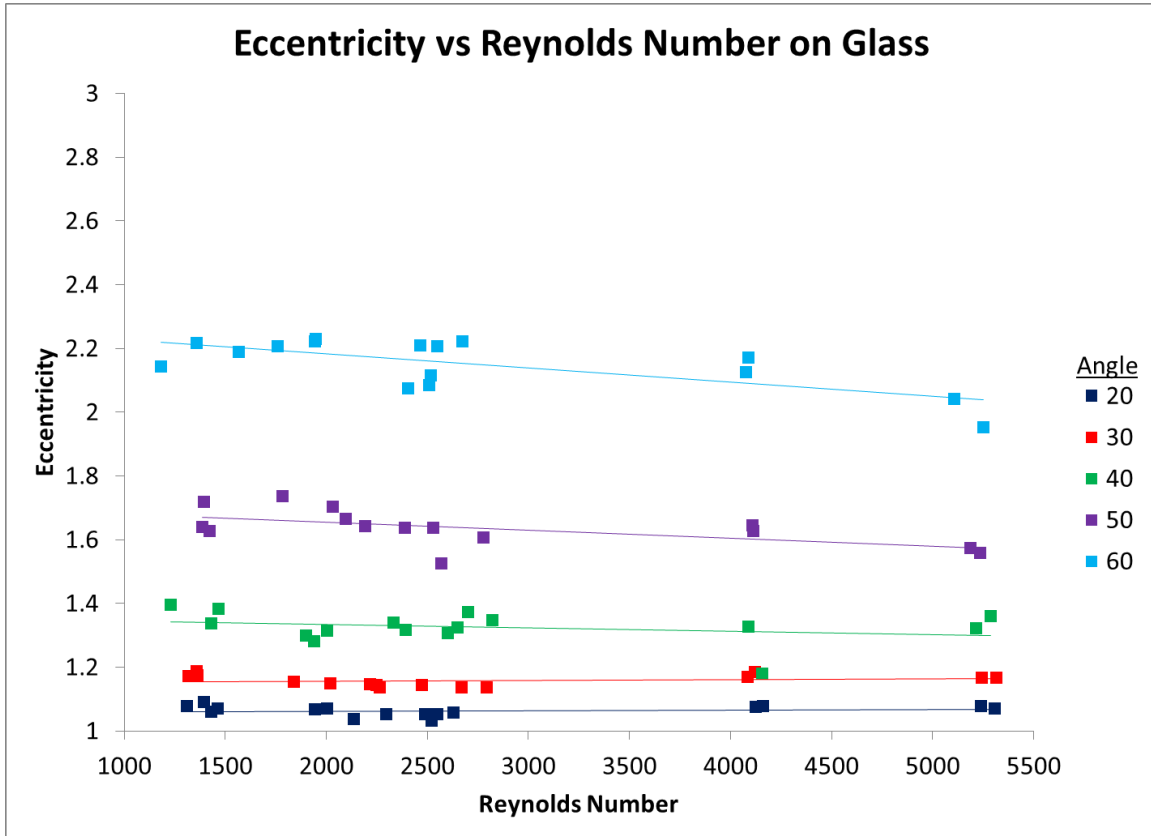
Figure 18. Eccentricity vs *Re* for impacts on glass.

Table 4. Slopes of eccentricity vs *Re* for impacts on glass.

Angle	Slope
20	2.02E-06
30	2.22E-06
40	-1.05E-05
50	-2.51E-05
60	-4.44E-05

Based on the results presented in Figure 18 and Table 4, *Re* appears to have little

effect, if any, on eccentricity until impact angles above roughly 40° are encountered.

Visually, there is a nearly imperceptible change in eccentricity as *Re* is increased from

1000 to 5500 for angles of 20°, 30°, and 40°. This is confirmed when looking at the

slopes. At 40° a change in *Re* of 5000, the entire range of experimentation, is needed for just an increase in eccentricity of 0.05. This is even more pronounced at smaller angles. On the other hand, a slight dependence is observed at higher angles. As Reynolds number is increased, the observed eccentricity decreases. This is somewhat counterintuitive. A drop moving at higher speeds should spread further when a more oblique force is applied. The impacting material exerts a normal force on the drop perpendicular to its orientation. This force decreases as the angle of inclination increases and it might be expected that the drop spreads further in the "downstream" direction under this condition; however, this is not the case. This suggests that something is acting tangentially to slow spreading at higher-angled impacts. The discussion will be continued in more detail at the end of Section 4.1 after considering impacts on other materials.
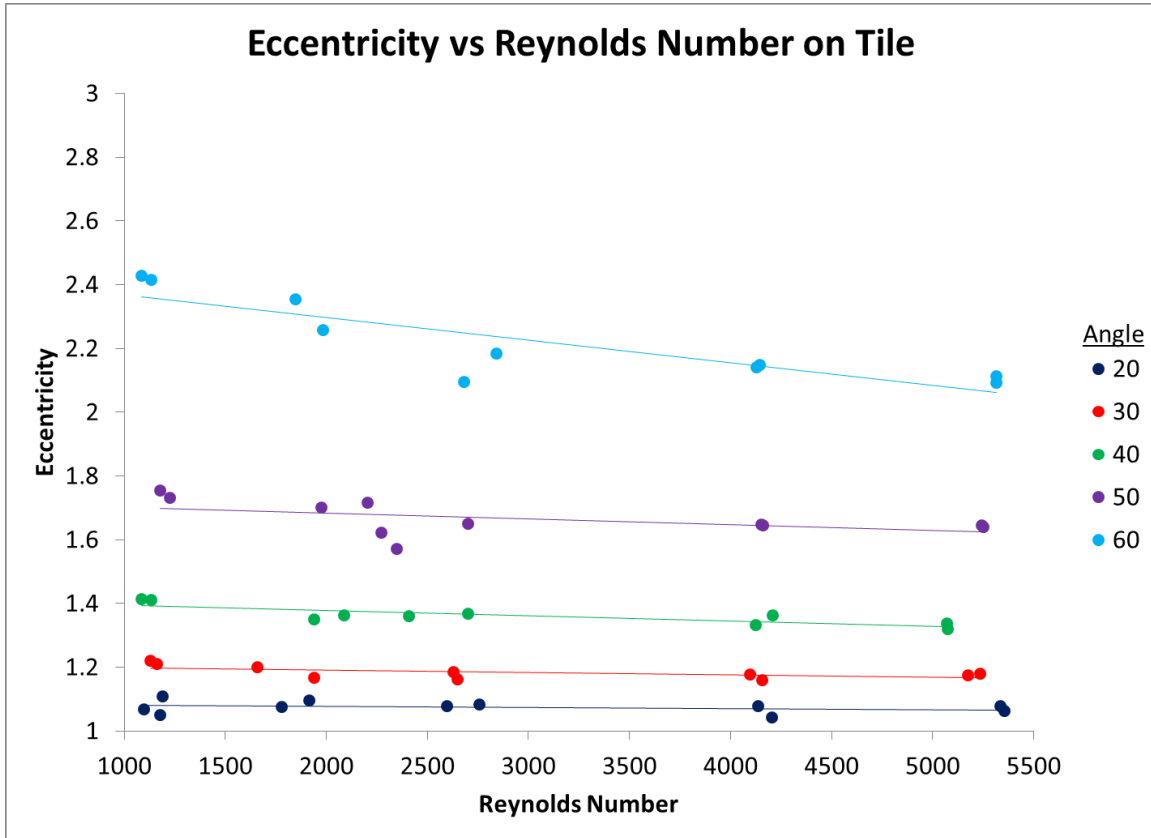
Figure 19. Eccentricity vs *Re* for impacts on Tile.

Table 5. Slopes of eccentricity vs Re for impacts on tile.

Angle	Slope
20	-3.23E-06
30	-7.98E-06
40	-1.69E-05
50	-1.84E-05
60	-7.11E-05

The pattern for eccentricity versus *Re* for impacts on tile seen in Figure 19 is very similar

to what was observed for impacts on glass. Both materials are hard, non-porous and

minimally rough, especially when compared with paper. The difference in surface

35

roughness, does not change the effect of *Re*, as clear stratification is seen at each angle

with minimal change in eccentricity as *Re* changes, at least until large angles. Again, at

60° a slight downward trend is observed. In examining the slopes shown in Table 5, the

magnitude of the slope at 60° is almost four times greater than that for 50°, meaning that

over the range of experimental *Re* values a meaningful change is observed in

eccentricity. Before discussing the cause of this trend, impacts on paper shown in Figure

20 and Table 5 are examined for behavior consistent with that observed so far.
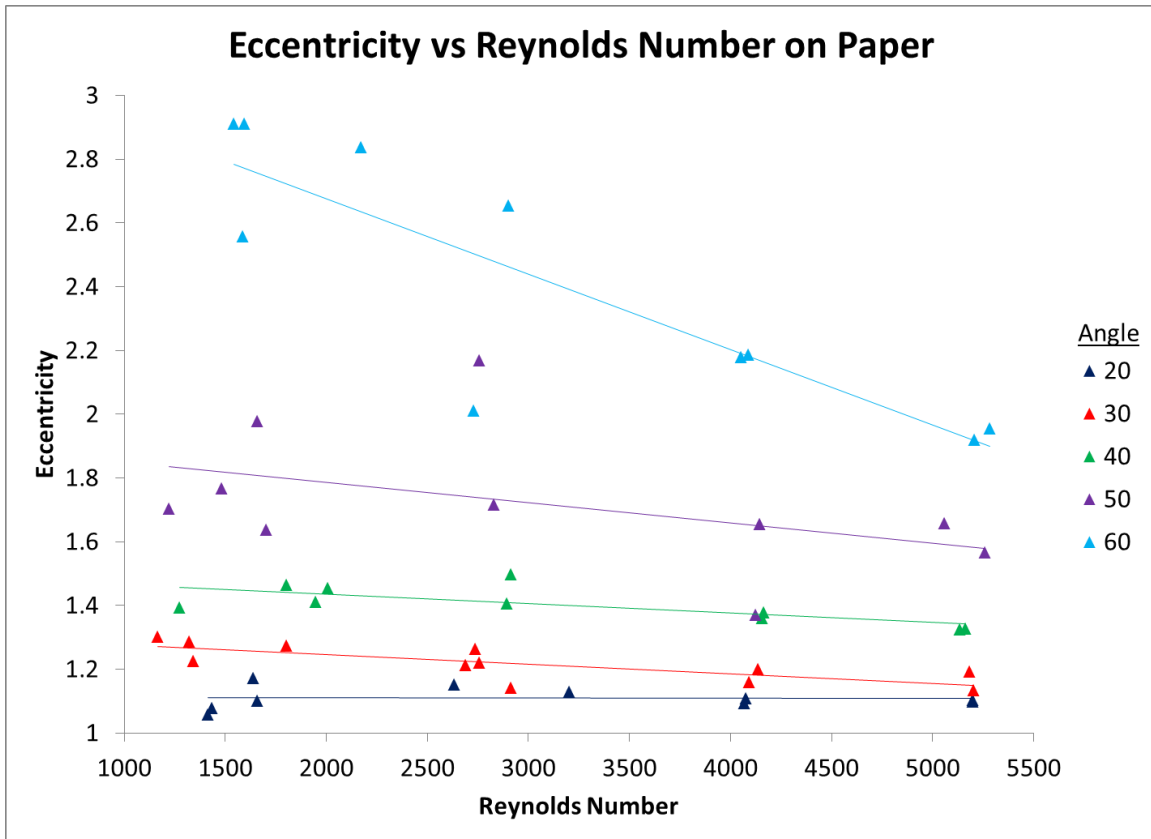
Figure 20. Eccentricity vs Re for impacts on paper.

Table 6. Slopes of eccentricity vs Re for impacts on paper.

Angle	Slope
20	-4.86E-07
30	-2.98E-05
40	-2.92E-05
50	-6.37E-05
60	-2.36E-04

Although the results for impacts on paper are more varied than for those on glass and tile, the trends remain the same. At small angles, *Re* has a minimal effect on eccentricity while at large angles the effect of *Re* is much more pronounced. In fact, at 60°, for the first time a significant change is observed in eccentricity as *Re* increases, suggesting that roughness plays a role in reducing eccentricity. By studying the contact line motion during spreading, this result begins to be explained. For low-*Re* impacts, spreading is a smoother process, with the lamella remaining mostly intact throughout the process. The spreading is slow enough that the rate that the contact line advances matches the rate of spreading of the bulk liquid. At higher *Re,* the bulk liquid attempts to spread more quickly than the contact line, the motion of which is opposed by surface roughness. This contrast results in the ejection of satellite drops, and the formation of liquid tongues and cast-forward features. Examples of these features are shown in Figure 21. Greater surface roughness further exacerbates this effect. Glass predominantly forms a cast-forward feature, while tile and paper often form tongues. The cast-forward feature is less disruptive to bulk contact line motion than tongue formation and results in a lesser effect on eccentricity. The greater roughness of paper compared to tile causes more abrupt changes in the drops forward edge and subsequently further effects eccentricity.
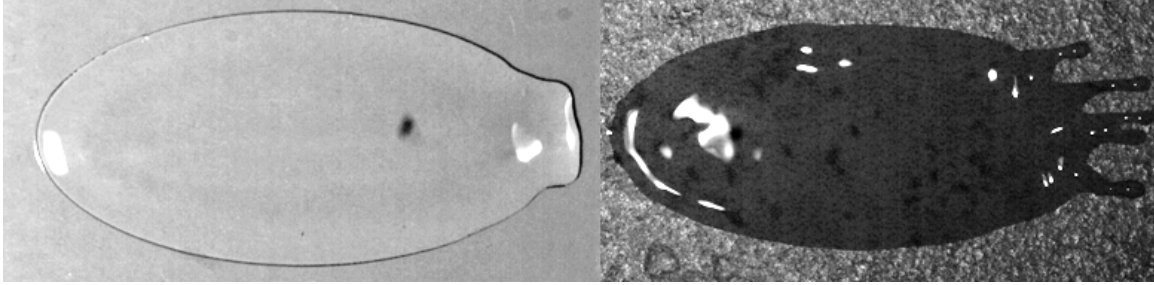
Figure 21. Illustration of tongues (right) and cast-forward (left) features. The right image is a high-*Re*, 60° impact on tile and the left image is a high-*Re*, 60° impact on glass.

Next, the effect of *La* on eccentricity is evaluated. *La* effects are identical to those of Re. For ease of viewing, data for glass and tile have been condensed onto a single plot in Figure 22. The same trends are seen as observed with *Re*. Low angles still exhibit minimal dependence on *La*, while high angles begin to show some effect. When looking at the impact results for paper shown in Figure 23, there is a similar decrease in the consistency of eccentricity and again high-angle impacts show a significant variation with *La*. It is reasonable to speculate that the trends in *La* are caused by the same reasons as those observed for *Re*. Increases in *La* correspond to increases in *Re*. In fact, they increase in a proportional fashion. Both dimensionless numbers are linear functions of droplet diameter. Thus, when droplet diameter causes certain effects, these effects should be seen in both *Re* and *La*.
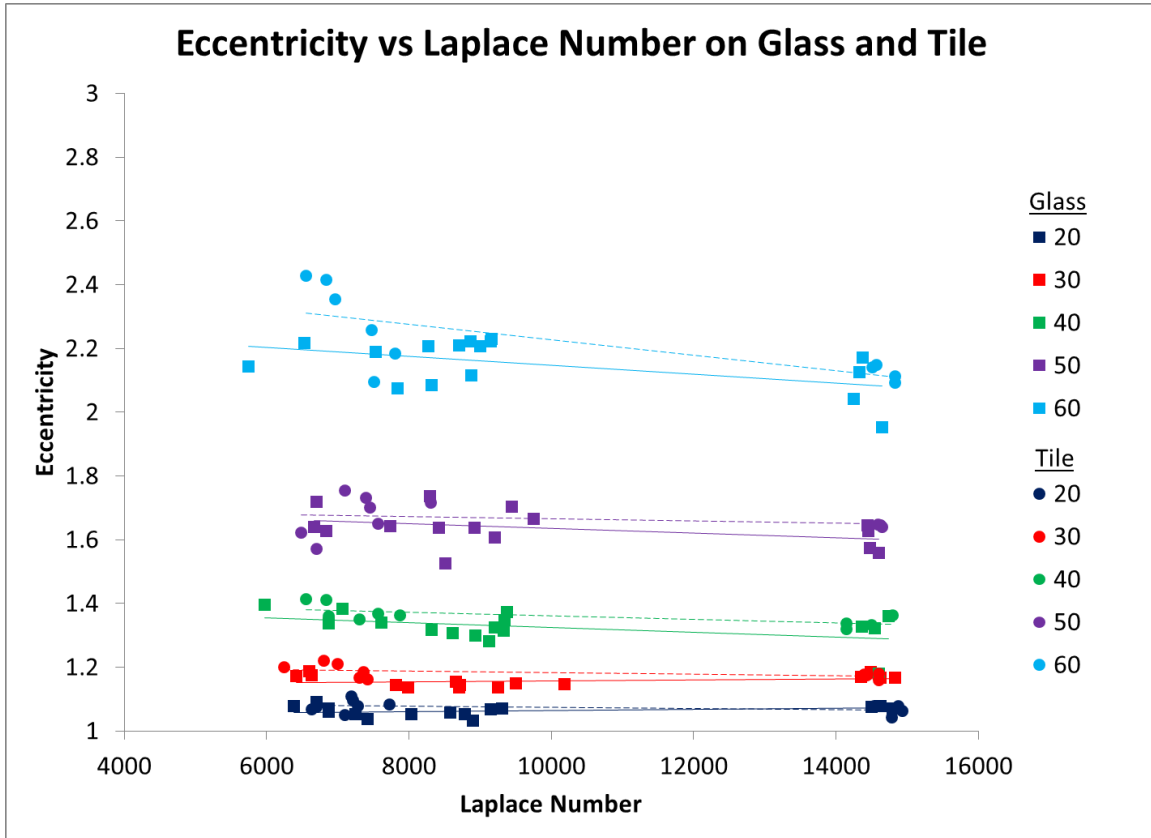
Figure 22. Eccentricity as a function of *La* for impacts on glass and tile. The dotted best fit curves are for tile and the solid lines are for glass. The gap between Laplace numbers of 10000 and 14000 is a result of a limited selection of orifice diameters used to produce droplets.

Table 7. Slopes of eccentricity vs La for impacts on glass and tile.

Angle	Glass	Tile
20	1.56E-06	-1.84E-06
30	1.49E-06	-2.61E-06
40	-7.38E-06	-5.68E-06
50	-7.28E-06	-3.51E-06
60	-1.41E-05	-2.41E-05
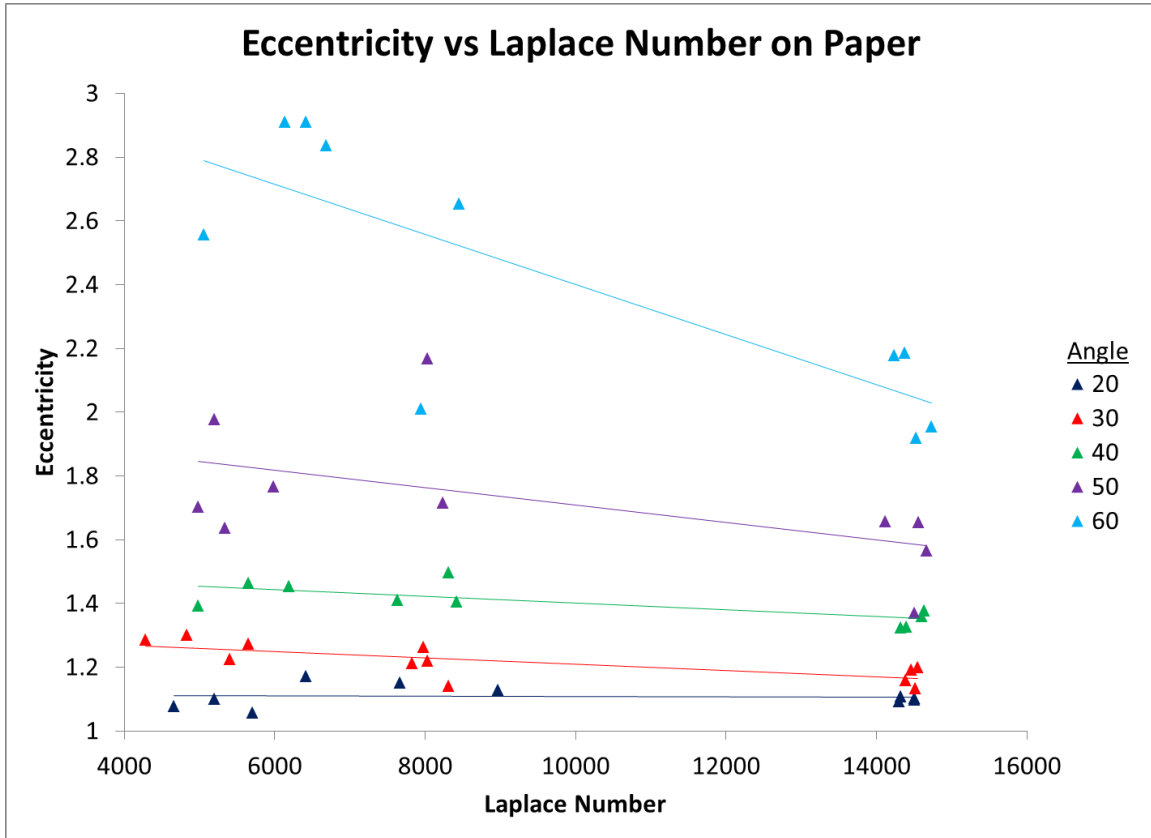
Figure 23. Eccentricity as a function of La for impacts on paper.

Table 8. Slopes of eccentricity vs La for impacts on paper.

Angle	Slope
20	4.01E-07
30	-1.01E-05
40	-1.06E-05
50	-2.74E-05
60	-7.85E-05

After considering the effects of *Re* and *La*, the effect of impact angle is investigated.

Figure 24 shows how eccentricity changes as a function of impact angle. Since similar

trends were seen in each material when investigating *Re* and *La*, they are shown on the same plot. Additionally, data are shown without distinguishing between changes in *Re*. Although this is fine for smaller angles, it must be kept in mind that *Re* was shown to have an effect on eccentricity for angles greater than 40°. Also indicated on the figure is a curve representing common practice in the forensics community.
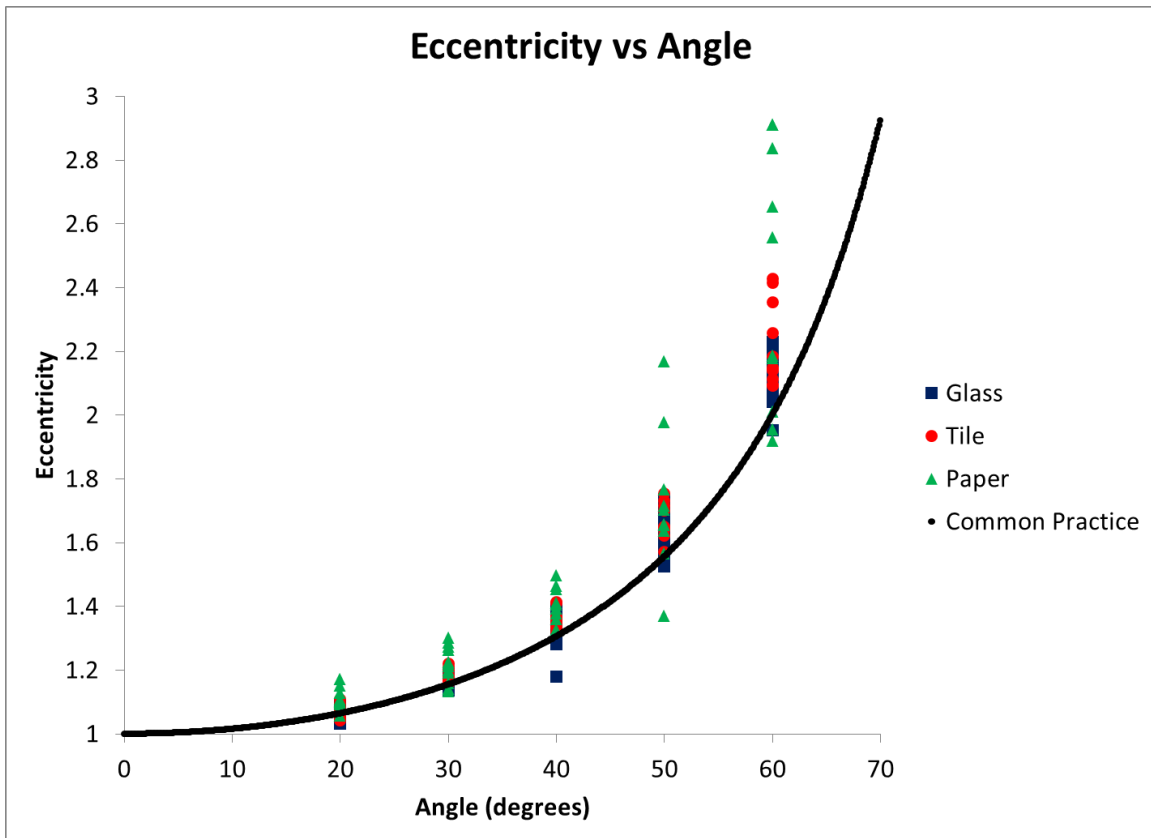
Figure 24. Eccentricity as a function of angle for impacts on glass, tile and paper. Data is also compared to a common practice curve.

Although the shape of the common practice curve somewhat reflects the data, it represents a crude approximation for high impact angles, differing by roughly 50% for impacts on paper at 60°. Adjustable parameters can be added to the common practice

equation as shown in equation (4.3), where A, B and C are unknown constants to be determined. By modifying these constants, the same type of regression is used, while shifting it to better fit the data. The data from the present experiments have been fit by minimizing the error in the sense of least-squares. Best-fit parameters are calculated for each material and are shown in Table 9. Figure 25 shows how the best-fit curves compare with each other.

$$\varepsilon = \frac{A}{\cos(\theta + B)} + C \qquad (4.3)$$

Table 9. Best fit values of parameters A, B and C for each material.

	A	B	C
Glass	0.9745	0.0541	0
Tile	0.9846	0.0650	0
Paper	0.6886	0.1902	0.3073
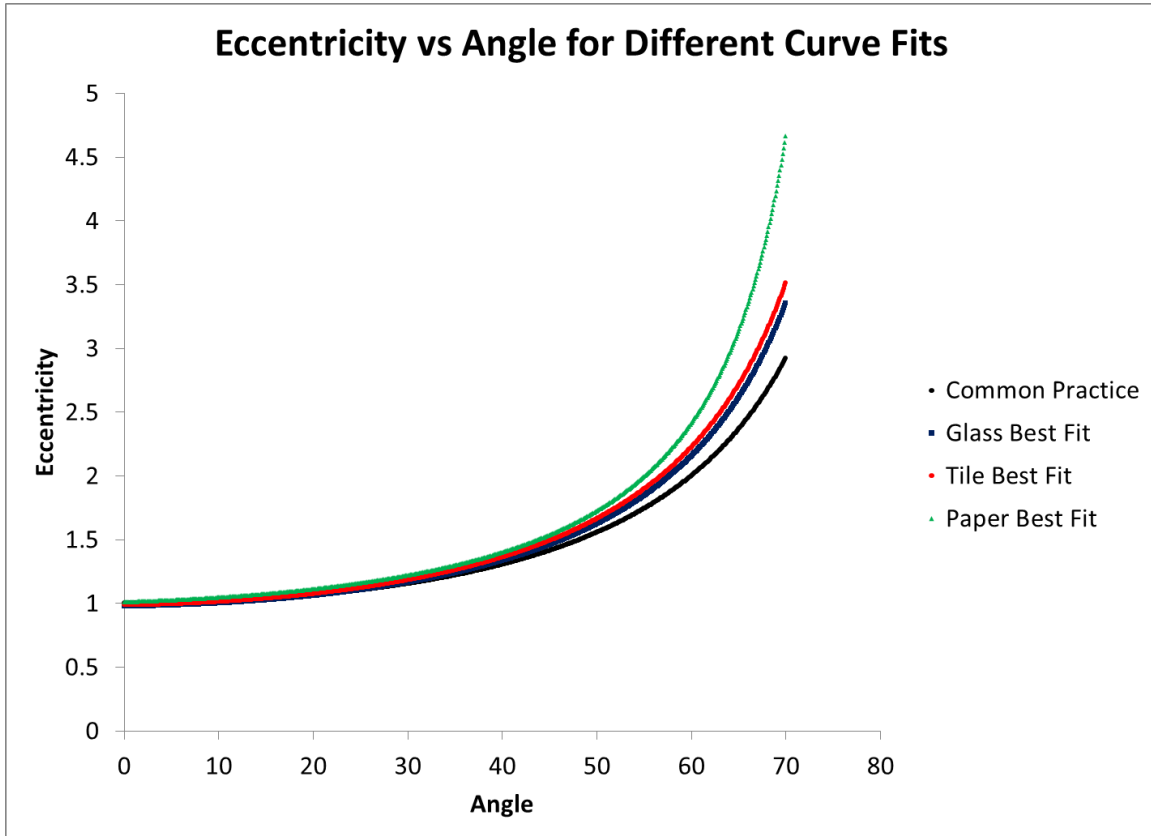
Figure 25. Eccentricity versus impact angle model comparisons.

What is observed is that for small to moderate angles and for the entirety of the glass and tile curves, the fits are practically identical. At the point of greatest separation, the predicted eccentricity of glass and tile differ by just 4.5%. At large angles the fit for paper diverges significantly from that of the others, but so too does the behavior, as discussed earlier. Neglecting high-angle impacts on paper, it is pertinent to question whether a single data fit has the ability to adequately predict angle based on eccentricity. Using all available data from impacts on glass and tile and data from impacts on paper up to 50°, a correlation was developed that is shown in Figure 26 along with material-specific ones. This curve lies nearly on top of the one for impacts on glass, and is just 4.3% different for impacts on tile at 70°, the point of maximum separation. This

correlation will be further evaluated in Section 4.4. Following Figure 26, the discussion

turns to the next parameter of interest, spread factor.

Table 10. Best fit values of parameters A, B and C for each material compared to the comprehensive curve.

	A	B	C
Glass	0.9745	0.0541	0
Tile	0.9846	0.0650	0
Paper	0.6886	0.1902	0.3073
Comprehensive	0.9978	0.0499	0
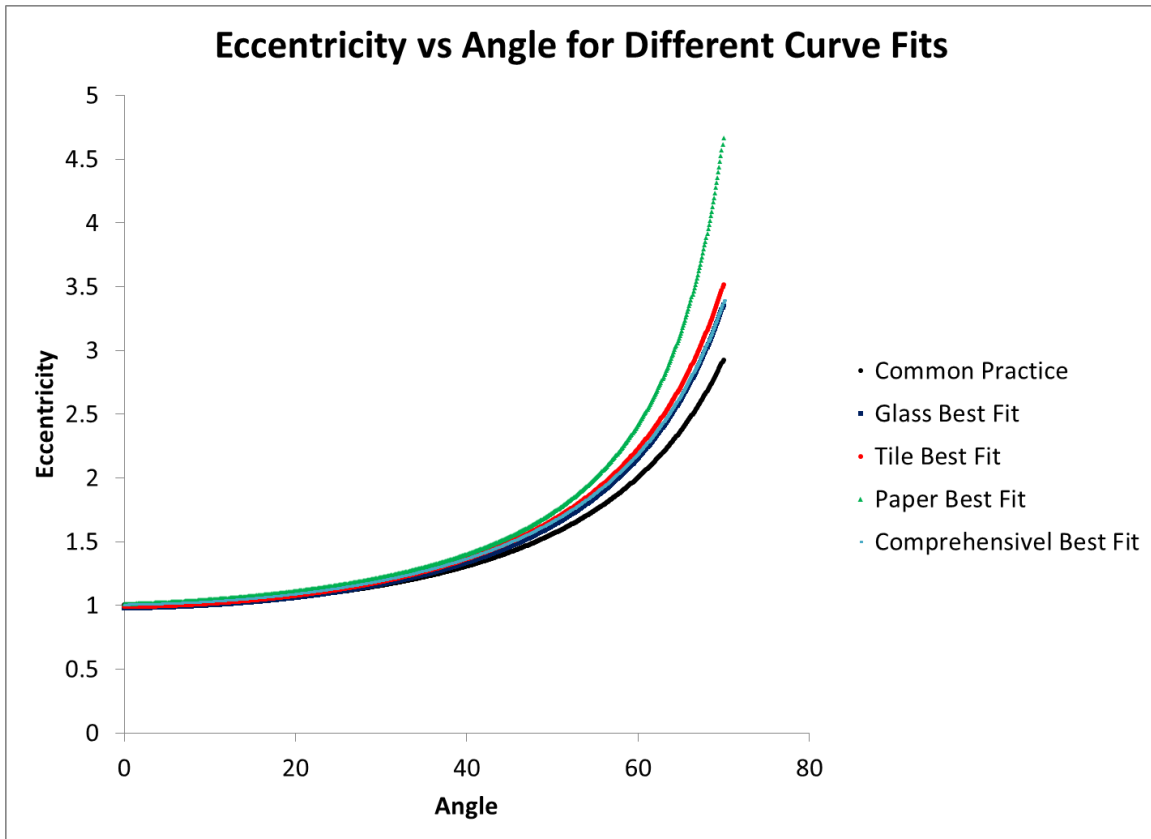
Figure 26. Eccentricity versus impact angle models compared to a comprehensive model.

4.2 Spread Factor

Recall that spread factor is the ratio between the area of a stain and the cross-sectional area of an incoming drop. Similar to eccentricity, contact line behavior is crucial to understanding and quantitatively evaluating spread factor. In order to understand contact-line motion and the factors involved, spread factor can be evaluated against Re, and impact angle. Figure 27 shows data for impacts on glass. The scale and the best fit curve are identical on each plot because best fit curves were created using the entire data set, not individual angles. The best fit curve is of the form shown in equation (4.4), where A and B are fitting constants.

$$SF = A(\mathrm{Re}^B) \tag{4.4}$$

Good agreement is evident across the data set with an R^2 value of 0.895 and at each individual angle with the average percent error of each angle ranging from 5 - 8.5%. If best fit curves are generated for each angle, the percent errors are within 5 - 8%, suggesting that the error is caused by measurement uncertainty and not by lack of accuracy of the best-fit curve. This suggests that there is minimal dependence between spread factor and angle. If a single curve can describe behavior across a range of values then that value must not be affecting behavior significantly.

Table 11. Fitting parameter values for spread factor against Re.

	Glass	Tile	Paper
A	0.2018	0.2568	1.707
B	0.5841	0.5490	0.299
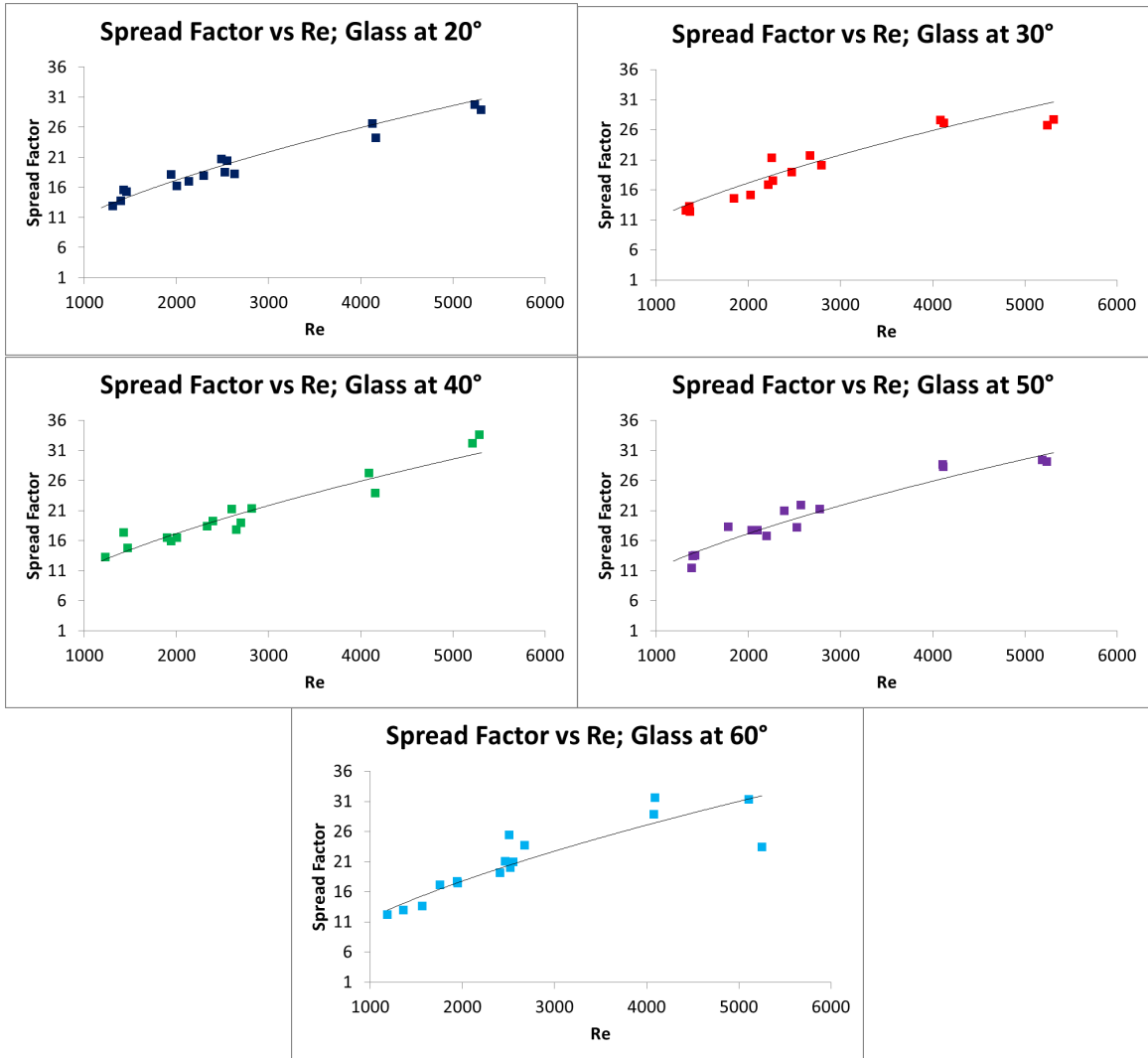
Figure 27. Spread factor as a function of *Re* for impacts on glass at various angles.

Figure 28 shows the same information as Figure 27 for impacts on tile; however, the curve fit to the entire data set does not accurately model the behavior at each individual angle. In this case, correlations for each individual angle fit the data significantly better, indicating that some dependence on angle may be evident. This is examined further in Figure 29.
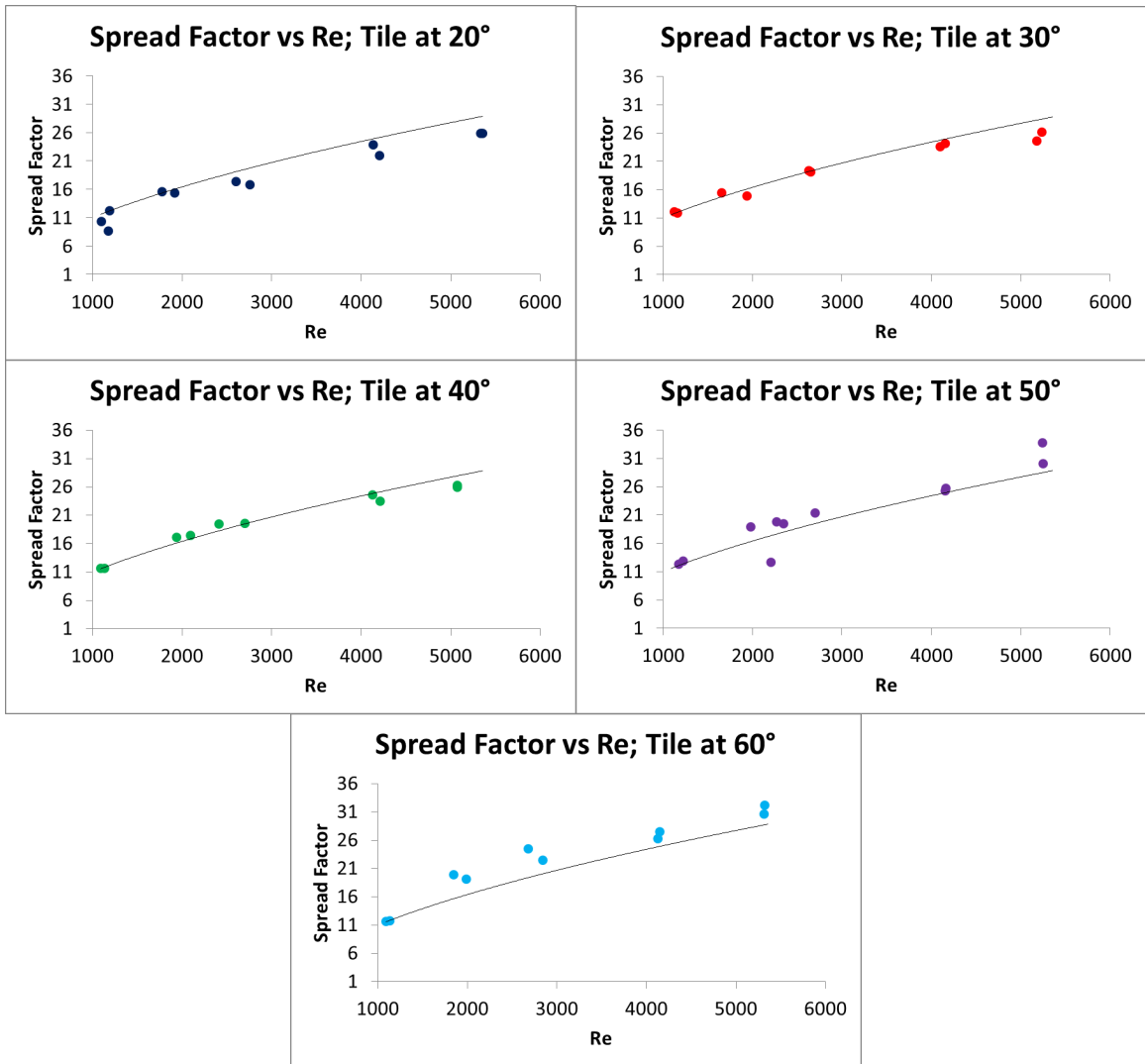
Figure 28. Spread factor as a function of *Re* for impacts on tile at various angles.
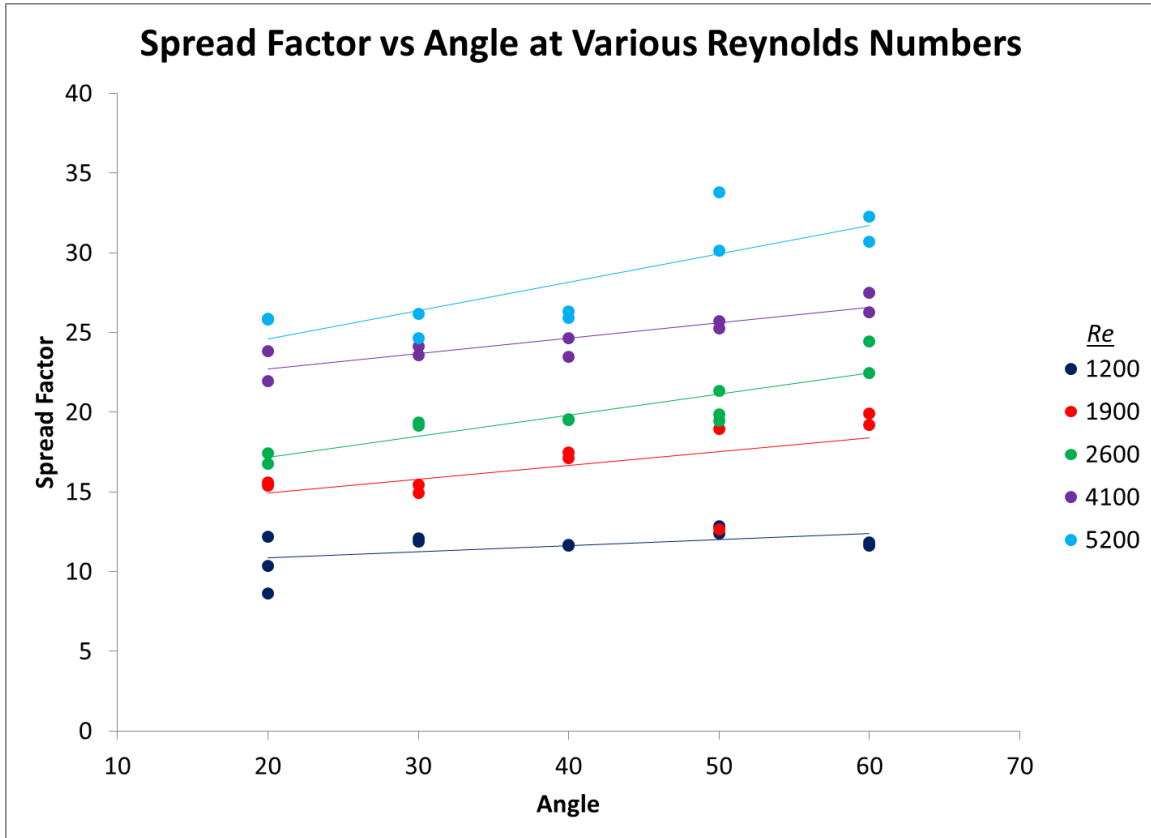
Figure 29. Spread factor as a function of angle for impacts on tile and increasing *Re*.

Although there is evident stratification, illustrating a clear trend in spread factor versus *Re,* at each *Re*, a slight upward trend is seen. By examining the slopes of the best fit lines, shown in Table 12, the significance of this trend can be quantified.

Table 12. Slopes of *Re* vs angle best fit curves on tile.

Re	Slope
1200	0.0380
1900	0.0872
2600	0.1322
4100	0.0963
5200	0.1776

At small *Re* the slope is such that changes would need to be on the order of the entire range of angles tested for a change in spread factor to be significant. In contrast, at high *Re* a change in 10° causes spread factor to change by 1.776. Thinking back to the investigation of eccentricity, recall that at high *Re* and high angles on rough surfaces, spreading in the direction of flow is inhibited, due to the formation of flow features such as tongues and cast forward. Now, evidence suggests that, at high *Re*, for a moderately rough surface, spreading is greater. The combination of these findings implies that spreading in the transverse direction is promoted for high-*Re*, high-angle impacts on rough surfaces. This could happen because liquid flows along the path of least resistance. Since spreading is inhibited in one direction, it is promoted in the other. Impacts on paper are presented in Figure 30 to see if this trend persists on other surfaces.
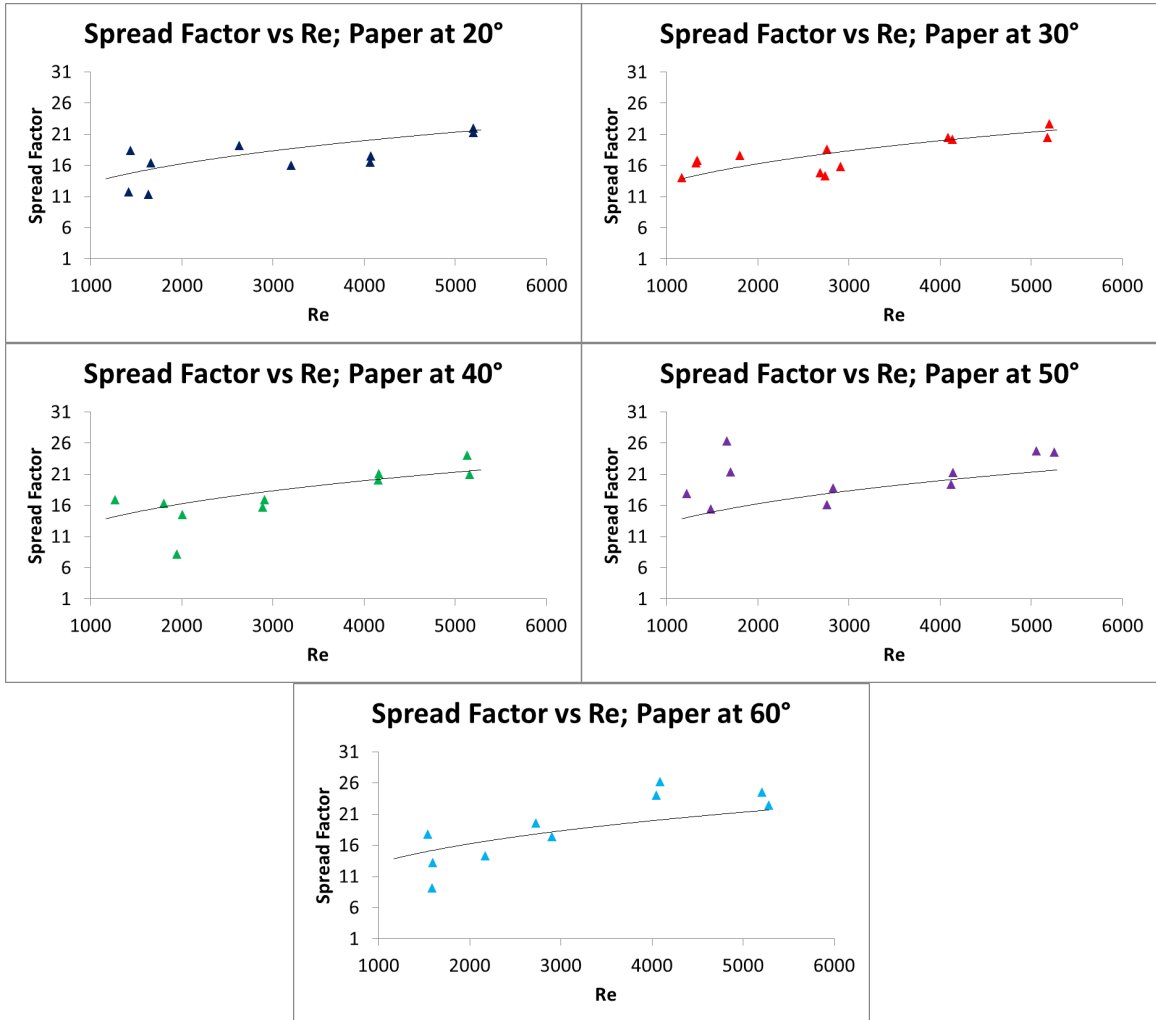
Figure 30. Spread factor as a function of *Re* for impacts on paper.

For impacts on this surface, much less regularity is evident, but there does not seem to be dependence on angle. Correlations for individual angles do not better represent the data than the general curve. Greater surface roughness on paper compared with glass and tile results in a much higher frequency of contact line pinning. As a drop spreads, certain points on the contact line are caught by roughness elements of the surface, reducing the ability of the contact line to move. The smoother glass and tile surfaces

50

have fewer impediments to spreading, the result being a more predictable relationship between the stain size and the incoming velocity and droplet size. The greater roughness of paper is also why a transverse spreading effect is not seen as with impacts on tile. With each surface manifesting different behavior, modeling spread factor with a single correlation is impractical. The size of a stain has many nuances that must be accounted for and simplifying the behavior leaves out important parameters. Within the context of forensic analysis, this means that many of the correlations that are applied in the field are done so incorrectly. Very rough materials, such as the paper used in this test procedure, are likely to give erratic results. Moderately rough materials show some response to changes in angle. Only for very smooth surfaces do spread factor correlations appear to have general applicability.

4.3 Spines and Satellites

The final parameter of particular interest is the number of spines. Counting spines is somewhat prone to interpretation. Spine definition must be explicit and consistently applied. The definition adhered to in this thesis is that a spine is a disruption, where a clear convex outline is seen. For clarity, Figure 31 demonstrates some of the ambiguity in deciding what constitutes a spine.
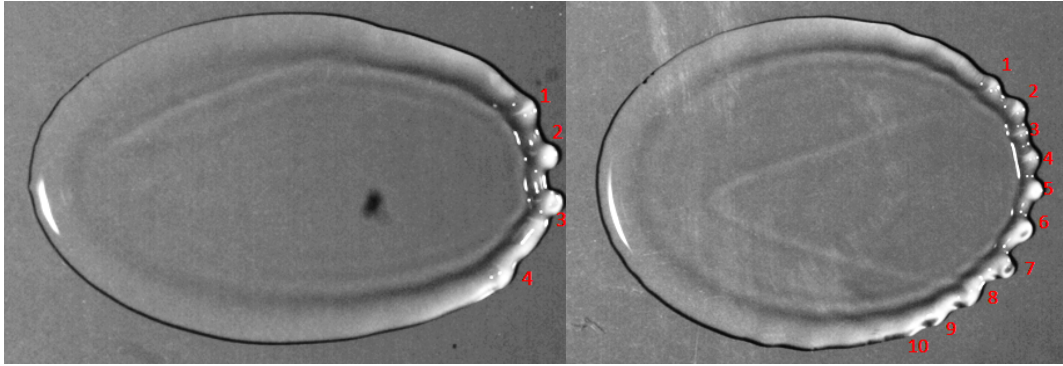
Figure 31. Illustration of how spines are counted. Consistency with regard to spine counting is very important. Both images are impacts on glass with $Re \approx 4000$. The left image is for an impact angle of 50°. The right is for an impact angle of 30°.

Spine correlations are complicated by the fact that they are based on two independent parameters: angle and Reynolds number. As the Reynolds number is increased the lamella is increasingly unstable and the number of spines increases. However, as the angle of impact increases, spine formation is suppressed on a greater portion of the circumference, as seen in Figure 31. The result of a two-variable dependence is that correlations are needed that can account for both parameters of interest.

An additional complication arises for spine formation on glass. Spine formation is based on Re as will be illustrated in the following plots, but roughness elements can also trigger this formation. With a smooth glass surface, there is little roughness to trigger spine formation and the number of spines versus Re and the impact angle is not consistent. In the case of low-Re impacts, a single spine or no spines was a common occurrence. Under these conditions, the conditions at impact can only be determined from the size of the stain. Figure 32 shows how the number of spines changes with Re for impacts on glass. Although, in general, the number of spines increases as Re increases and

decreases as the impact angle is increased, there is large uncertainty. Best fit curves are not shown in Figure 32, because with glass, the fit of these curves is poor. Typical R^2 values for these curves are 0.4-0.6. This is of concern because spine counts have become a crucial part of crime-scene reconstruction. On smooth surfaces, their use is unreliable. Figure 33 and Figure 34 show the same information for impacts on tile and paper.
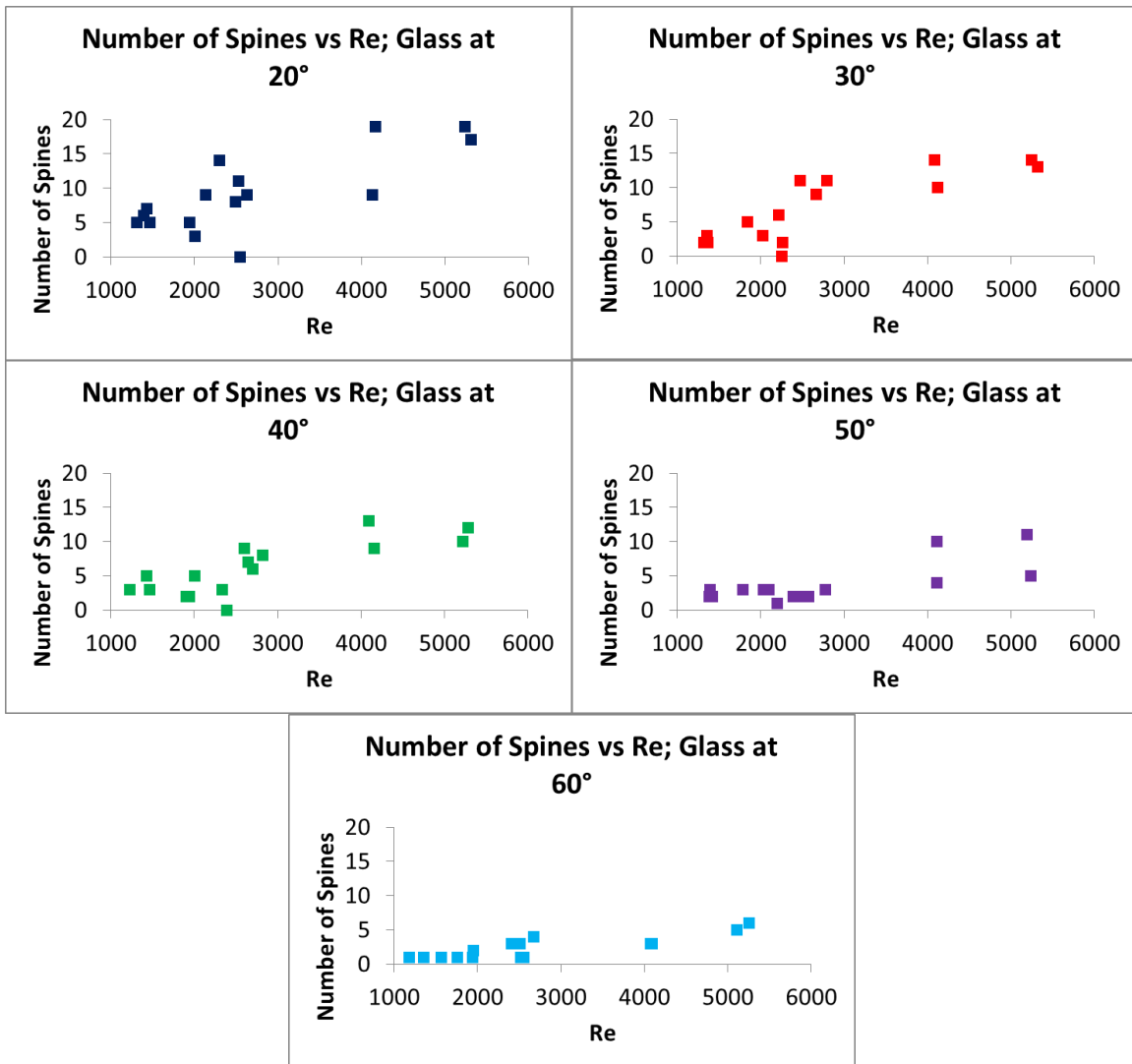
Figure 32. Plot of the number of spines as a function of *Re* for various impact angles on glass.
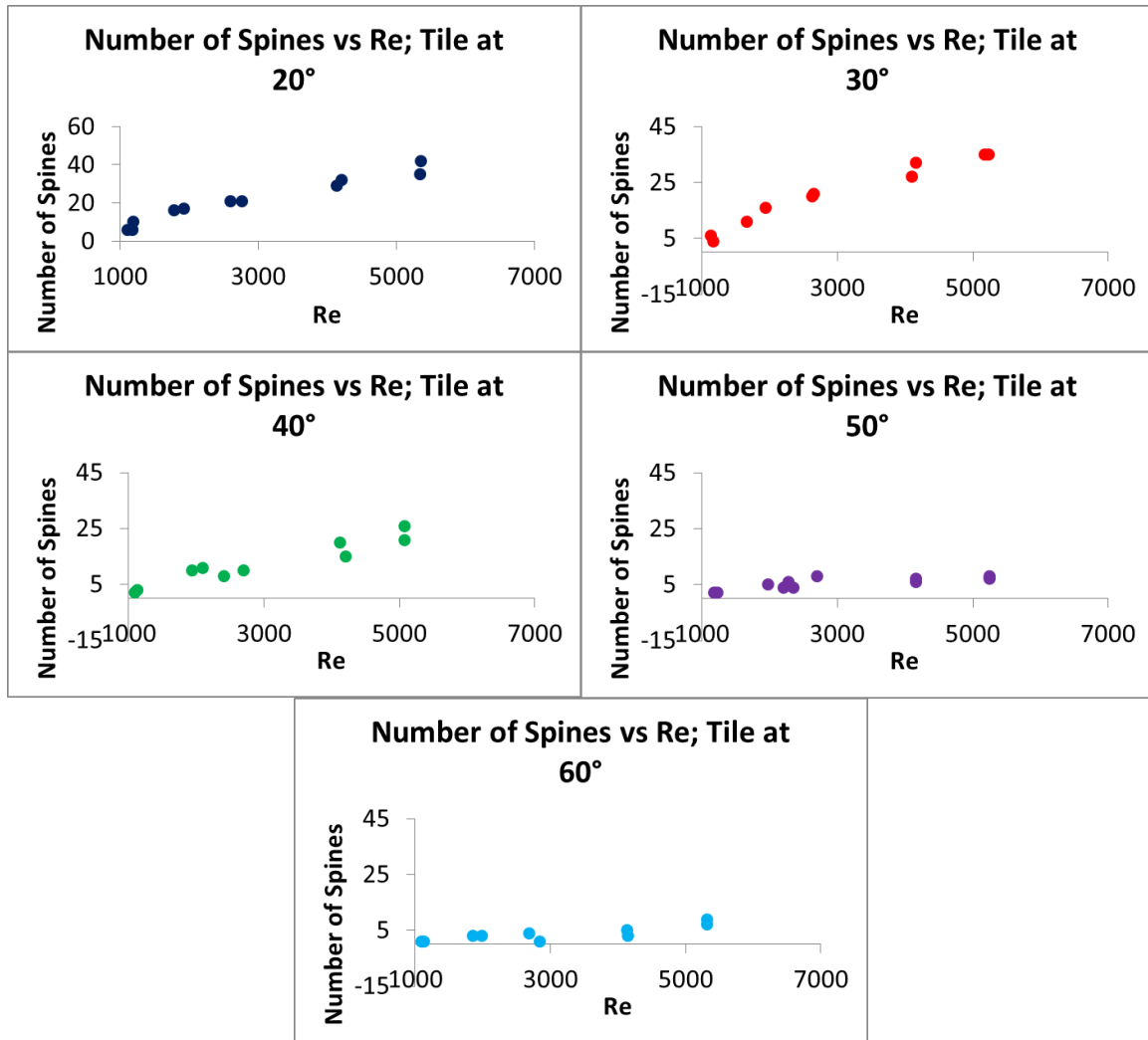
Figure 33. Plot of the number of spines as a function of *Re* for various impact angles on tile.
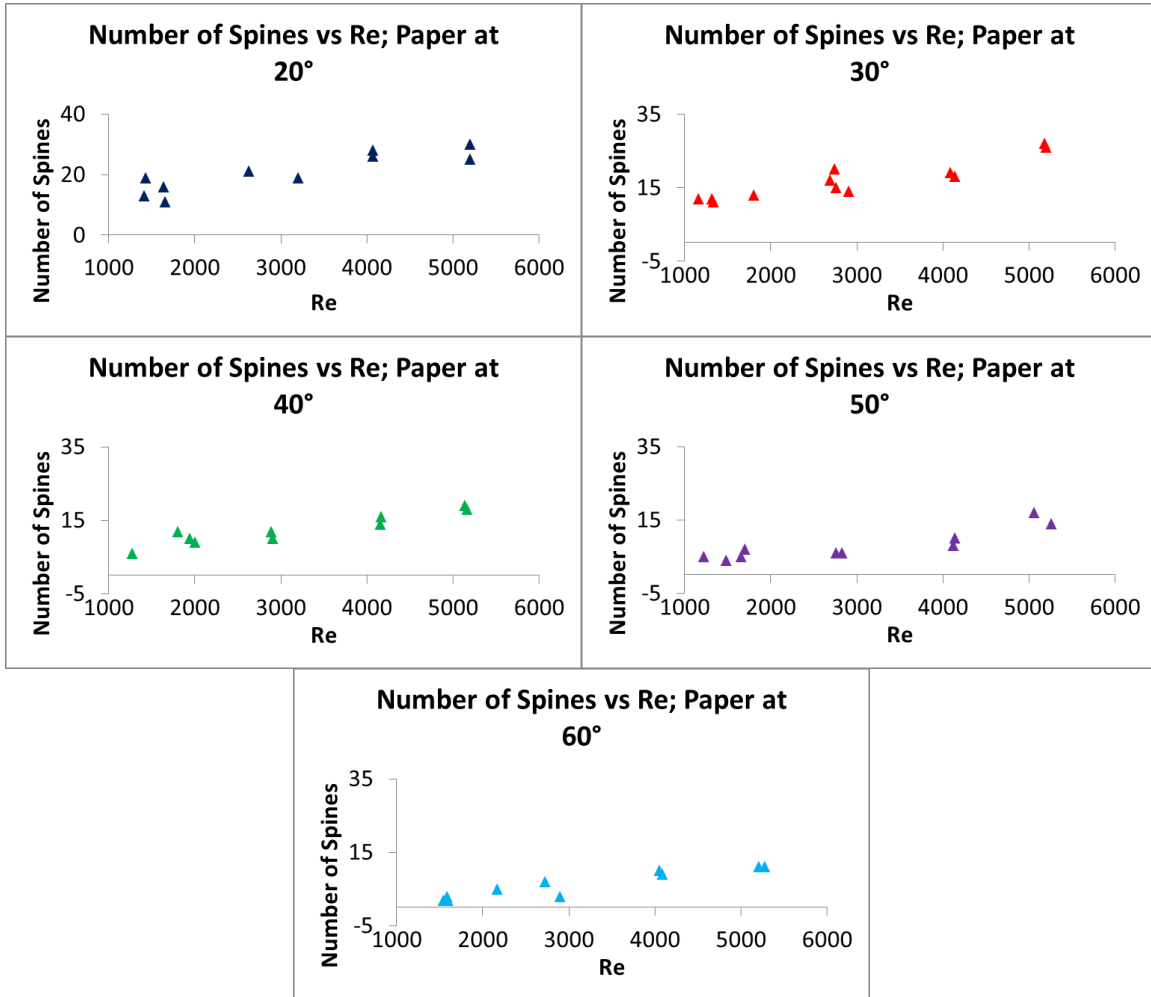
Figure 34. Plot of the number of spines as a function of *Re* for various impact angles on paper, along with best fit curves for each angle.

For tile and paper, spine formation is more consistent. We see the same trend as with glass, namely, increasing the angle decreases the expected number of spines, while increasing *Re* increases this value. More consistent behavior can be attributed to surface roughness. Roughness acts as a trigger for lamellar instabilities. For impacts on tile and paper, predicting *Re* based on the number of spines and the predicted impact angle would appear to be feasible. Adam [4] postulated a relationship between the

number of spines, the impact angle and Re of the form shown in equation (4.5), where A and B are fitting parameters.

$$N = Re^A \cos(\theta)^B \qquad\qquad (4.5)$$

Fitting parameter values are shown in Table 13. Figure 35, shows the best fit curves for tile and paper. Glass is not shown because of the erratic nature of the results.

Table 13. Fitting parameter values for number of spines against Re and impact angle.

	Glass	Tile	Paper
A	.3078	.4351	.3991
B	2.3090	3.309	2.1733
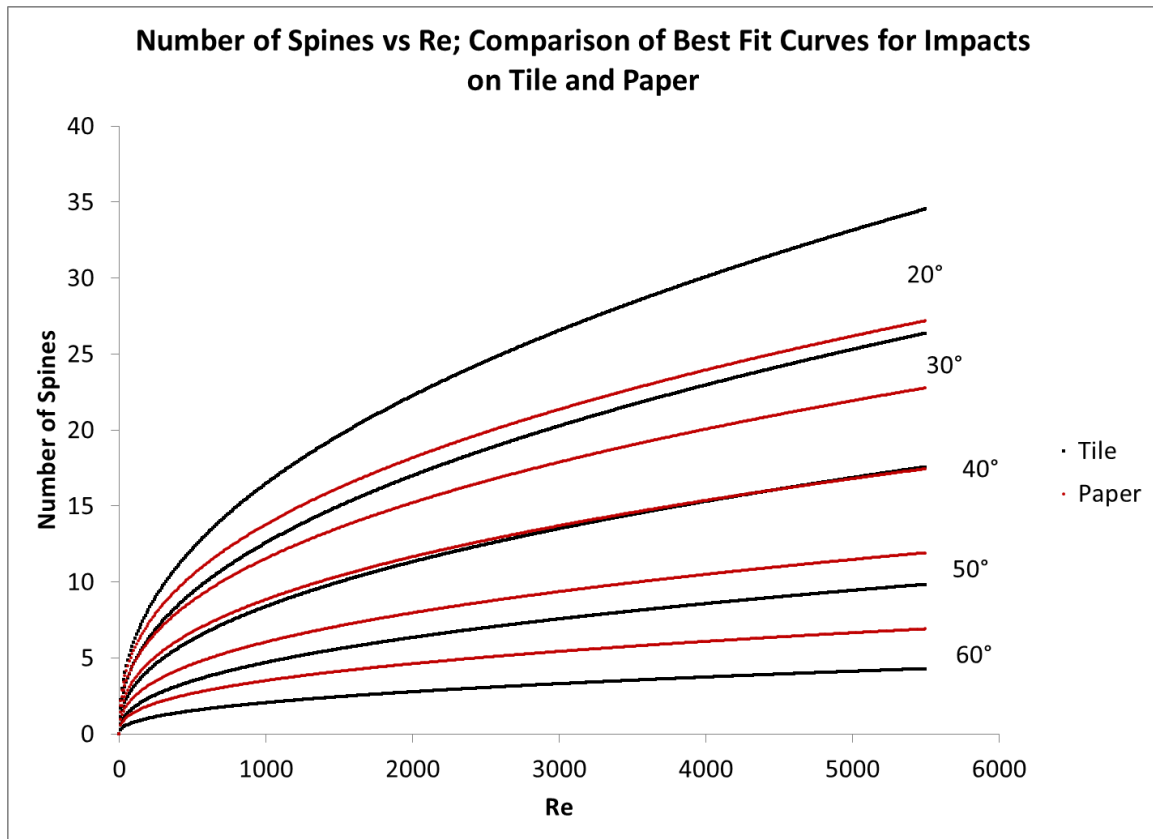
Figure 35. Best fit curves comparison between tile and paper.

Based on the best fit curves for tile and paper, the numbers of spines at an impact angle of 40° are nearly identical, but the curves differ at all other angles. At high impact angles, paper exhibits more spine formation while at low angles tile does. This outlines the competing effects of lamellar stability and the inhibition of spreading. Lamellar stability determines the number of spines formed along a certain length of the contact line; however, the length of the contact line is a factor in the total number of spines observed around the periphery of a drop stain. Roughness inhibits spreading, thus reducing the total number of spines, but also decreases the stability of the lamella, increasing the number of spines over small sections. At high-angle impacts, lamellar stability effects trump those of the reduction in spreading while at low angles the opposite occurs. The threshold value where one effect dominates the other appears to be at 40°.

It is interesting to note that the values for the fitting parameters A and B for tile nearly match those found by Adam [4], 0.44 and 3.3 versus 0.5 and 3.5. Adam [4] did not specify roughness or porosity for the type of paper used, other than to say it was non-porous. It is possible that the surface properties of the tile used in this experiment and the paper used in the study by Adam [4] are similar. This may explain the similarities. What is clear from this analysis is that the relationship between the number of spines, Re and impact angle is also affected by surface properties and any correlations developed between these parameters must take these into account.

4.4 Correlation Summary in a Forensic Context

In sections 4.1 - 4.3 specific parameters were studied against individual variables. Equally important as understanding how surface and kinetic properties affect spreading behavior is understanding how different properties fit together in the context of a forensics investigation. At a crime scene, three parameters are measured from a blood stain: the major diameter, minor diameter and the number of spines. From these three measurements the impact parameters of interest must be determined. This is done by running the measured parameters through a series of correlations. The first step is to calculate the angle of impact using equation (4.6).

$$\theta = arccos(\frac{0.9978}{\varepsilon}) - 2.8611 \qquad (4.6)$$

This correlation, developed in section 4.1, is valid across all of the materials tested at low angles and continues to be valid at high angles on smooth surfaces. By choosing drop stains on smooth materials with eccentricities of less than two, the accuracy of predicted impact angles is high. Next, the number of spines and the calculated angle are used to determine Re based on equation (4.7). Re is then used to determine spread factor based on equation (4.8).

$$N = Re^{A}\cos(\theta)^{B} \qquad (4.7)$$

$$SF = A(Re^{B}) \qquad (4.8)$$

Spread factor relates the stain area to the size of the incoming droplet. Since stain area is calculated with the measured major and minor diameters, the droplet size is determined next. Finally, using Re and the just-computed droplet size, the droplet speed

can be determined. Both equation (4.7) and equation (4.8) have fitting parameters that are based on the impacted material.

Table 14. Fitting parameter values for number of spines against *Re* and impact angle.

	Glass	Tile	Paper
A	0.3078	0.4351	0.3991
B	2.3090	3.309	2.1733

Table 15. Fitting parameter values for spread factor against *Re*.

	Glass	Tile	Paper
A	0.2018	0.2568	1.707
B	0.5841	0.5490	0.2990

Using equations 4.6 - 4.8 particular stains can be used to determine the conditions that led to their creation; however, it needs to be noted that not all stains can be used in this way. Eccentricty and spread factor information for very rough surfaces such as paper is unpredictable and smooth surfaces such as glass show significant spread in the number of spines produced. An ideal stain for obtaining information is one that is on a hard, moderately rough, non-porous surface. A forensic examiner must carefully evaluate surface properties before using any correlation deveolped in this thesis.

In order to evaluate the accuracy of the correlations laid out in equations 4.6 – 4.8, the information gathered in this experiment was run through these correlations to determine their accuracy. **Table 16** presents the average error of equations 4.6 and 4.8. on each surface.

Table 16. Average error of the correlations presented in equation 4.6 and equation 4.7.

	Glass	Tile	Paper
Average error of eccentricity (deg.)	1.92	1.36	3.35
Average error of diameter (mm)	0.11	0.13	0.18

Table 16 illustrates that equation 4.6 and equation 4.8 predict spreading behavior to a high degree of accuracy. Over all materials, equation 4.6 represents a 40% improvement in accuracy over the common practice curve. Greater variation is seen when predicting the impact angle on paper, as expected, but an average error of just 3.35° suggests that equation 4.6 is a useful relationship on this surface. Considering equation 4.8, the average error of the predicted diameter is based on already knowing Re of the impacting droplet. This error is only representative of the error in the spread factor correlation. Table 16 shows that equation 4.8 accurately predicts the size of the droplet. A forensic examiner would be able to determine the size of an impacting droplet to within approximately 0.12 mm for impacts on glass and tile. On paper the correlation is 33% less accurate, but remains able to predict behavior to an acceptable degree of accuracy.

In reality, the Reynolds number of an impacting droplet is not known and, in theory, should be found using equation 4.7. The average error associated with equation 4.7 for impacts on tile and paper (recall that impacts on glass showed too much variability) is 55% from the actual value. This means that a droplet with a calculated Re of 2000 would be expected to lie within the range of 1290 to 3100. In order to use the number of spines as a method for determining Re, the error associated with this measurement must be significantly reduced. Although an average error of 55% is better than making erroneous assumptions, such as using the "normal" drop volume technique, much more refinement

of this method is necessary. One possible method would be to correlate the wavelength or peridiodicity of spine formation to *Re* or *We*. It is possible that the distance between two spines better predicts the *Re* of the impacting drop than the total number of spines around the perimeter.

Chapter 5 - Conclusion

Droplet impacts were broken down into four stages and the case was made that the

spreading stage is the most important aspect for forensic purposes. Three specific

characteristics of droplet spreading were examined: eccentricity, spread factor and spine

formation. Eccentricity was found to be strongly dependent on the impact angle, and a

correlation was developed that was shown to be 40% more accurate than the common

practice curve. Reynolds number was found to affect eccentricity at high angles and for

rough materials. When spreading occurs quickly, as in the case of high-Re impacts, the

contact line moves more slowly than the bulk liquid due to surface roughness. When this

happens, instabilities of the lamella result in less spreading in the direction of flow,

resulting in a smaller eccentricity.

Spread factor was found to be largely independent of impact angle, but strongly

dependent on Re. Correlations were developed that compare spread factor to Re for

each material. As the surface roughness of a material increases, less spreading is

evident. Spreading on paper was more erratic than on either glass or tile. This was

attributed to the variability in surface roughness, and perhaps to porosity, although this

was not investigated. One interesting combination of parameters suggests that

spreading is promoted in the transverse direction for high-Re, high-angle impacts on tile.

Spines were shown to depend on Re, the angle of impact and the material substrate. An

equation was proposed that relates these three parameters. Fitting parameters were

calculated for each material and the best fit curves for paper and tile were compared.

Glass was left out of this comparison due to the poor representation of results by the best fit curve. This poor fit was attributed to the complete lack of surface roughness for glass. Spine formation is more consistent when surface roughness decreases lamella stability and acts as a trigger for spine formation. Glass and tile best fit curves were the same at an impact angle of 40°. At high-angle impacts paper shows more spine formation while at low-angle impacts tile shows more. This may be due to the competing effects of reduced lamella stability and the reduction of spreading, which are brought on by surface roughness. Surface roughness acts both as a trigger of spine formation and as an inhibitor of spreading. Spine formation increases over a portion of the lamella when lamella stability decreases; however, when less spreading is evident, the length of the contact line decreases, decreasing the number of spines. Which of these effects is more pronounced is dependent upon impact angle, where 40° appears to be the threshold at which both effects are equally important.

After analyzing spreading behavior in terms of forensically relevant parameters, an algorithm for obtaining parameters of interest from those measured was described in detail. A final set of correlations was presented, with fitting parameters for each material. These correlations include a corrected relationship between eccentricity and impact angle and the argument has been made that for an isotropic, minimally rough surface at small to moderate angles, this curve has wide-ranging applications. Also among the correlations developed are ones for spread factor versus Reynolds number and the number of spines versus the impact angle and Reynolds number. The best surfaces for examination are isotropic ones, with small to moderate roughness values.

These surfaces allow for predictable eccentricity and spread factor plus they trigger spine formation.

There are a number of avenues available for building upon the work presented in this thesis. The first is expanding upon the range of dimensionless parameters that were studied. Specifically, increasing droplet velocities would a logical next-step so that correlations could be developed for a more robust set of forensics conditions. Developing a droplet generator capable of producing drops at speeds greater than terminal velocity would be invaluable in this pursuit. In addition, more surfaces should be studied. Roughness can be studied in greater detail including more materials within the range studied here, investigating the effects of anisotropy on spreading and investigating surfaces with more uniform roughness, i.e. surfaces that have uniform roughness at the microscopic level. Additionally, the effects of porosity could be dealt with at greater length. The spreading behavior observed in this experiment was attributed mostly to surface roughness, but it is possible that the porosity of the paper used had a greater effect than is hypothesized here.

Appendix A - Uncertainty Propagation

To determine the error associated with each measurement, the equations shown below were used. This method was taken from Kline and McKlintock [18], whose method is based on a property being defined by its mean value (m) plus or minus the uncertainty (w) and the odds that the true value lies in this range is (b) to 1:

Measurement = m ± w (b to 1)

The uncertainty of each measured property shown in the following table was based on odds of 20 to 1.

Property	Symbol	Uncertainty	Units
Density	ρ	2.16	kg/m^3
Kinematic Viscosity	v	7.58E-9	m^2/s
Surface Tension	σ	0.00003	N/m
Distance (velocity calculation)	z	0.0000762	m
Time (velocity calculation)	t	0.0002	sec
Droplet mass	m	0.0004	g
Major diameter of stain	L	0.12	mm
Minor diameter of stain	W	0.12	mm
Velocity	V	Calculated	m/s
Drop Diameter	D	Calculated	m

$$Error(V) = \sqrt{(\frac{dV}{dz} \times \Delta z)^2 + (\frac{dV}{dt} \times \Delta t)^2} = \sqrt{(\frac{1}{t} \times \Delta z)^2 + (\frac{-z}{t^2} \times \Delta t)^2}$$

$$Error(D) = \sqrt{(\frac{dD}{dm} \times \Delta m)^2 + (\frac{dD}{d\rho} \times \Delta \rho)^2} = \sqrt{((\frac{2}{9\pi m^2 \rho})^{1/3} \times \Delta m)^2 + ((\frac{-2m}{9\pi \rho^4})^{1/3} \times \Delta \rho)^2}$$

$$Error(Re) = \sqrt{(\frac{dRe}{dV} \times \Delta V)^2 + (\frac{dRe}{dD} \times \Delta D)^2 + (\frac{dRe}{dv} \times \Delta v)^2} = \sqrt{(\frac{D}{v} \times \Delta V)^2 + (\frac{V}{v} \times \Delta D)^2 + (\frac{-VD}{v^2} \times \Delta v)^2}$$

$$Error(We) = \sqrt{(\frac{dWe}{dV} \times \Delta V)^2 + (\frac{dWe}{dD} \times \Delta D)^2 + (\frac{dWe}{d\rho} \times \Delta \rho)^2 + (\frac{dWe}{d\sigma} \times \Delta \sigma)^2}$$

$$= \sqrt{(\frac{2\rho VD}{\sigma} \times \Delta V)^2 + (\frac{\rho V^2}{\sigma} \times \Delta D)^2 + (\frac{V^2 D}{\sigma} \times \Delta \rho)^2 + (\frac{-\rho V^2 D}{\sigma^2} \times \Delta \sigma)^2}$$

$$Error(La) = \sqrt{(\frac{dLa}{dD} \times \Delta D)^2 + (\frac{dLa}{dv} \times \Delta v)^2 + (\frac{dLa}{d\rho} \times \Delta \rho)^2 + (\frac{dLa}{d\sigma} \times \Delta \sigma)^2}$$

$$= \sqrt{(\frac{\sigma}{v^2 \rho} \times \Delta D)^2 + (\frac{-2\sigma D}{\rho v^3} \times \Delta v)^2 + (\frac{-\sigma D}{v^2 \rho^2} \times \Delta \rho)^2 + (\frac{D}{v^2 \rho} \times \Delta \sigma)^2}$$

$$Error(\varepsilon) = \sqrt{(\frac{d\varepsilon}{dL} \times \Delta L)^2 + (\frac{d\varepsilon}{dW} \times \Delta W)^2} = \sqrt{(\frac{1}{W} \times \Delta L)^2 + (\frac{-L}{W^2} \times \Delta W)^2}$$

$$Error(SF) = \sqrt{(\frac{dSF}{dL} \times \Delta L)^2 + (\frac{dSF}{dW} \times \Delta W)^2 + (\frac{dSF}{dD} \times \Delta D)^2} = \sqrt{(\frac{4W}{D^2} \times \Delta L)^2 + (\frac{4L}{D^2} \times \Delta W)^2 + (\frac{-8LW}{D^3} \times \Delta D)^2}$$

Appendix B - Raw Data with Uncertainty

The following tables have been separated into two sections in order to fit on a page. The first section includes dimensional parameters angle, time, distance, velocity, mass and diameter along with their uncertainties. The second includes dimensionless parameters Reynolds Number, Weber Number and Laplace Number, as well as values that were determined via high-speed, namely, eccentricity, spread factor and the number of spines.

Data for impacts on glass

Video ID	θ (°)	Δθ (°)	t	Δt	z	Δz	V	ΔV	m	Δm	D	ΔD
00118	20	0.5	0.0059	2.00E-04	0.0235	7.62E-05	3.9831	1.36E-01	7.86E-06	4.00E-07	0.00239	4.062E-05
00119	20	0.5	0.0059	2.00E-04	0.0235	7.62E-05	3.9831	1.36E-01	1.07E-05	4.00E-07	0.00266	3.302E-05
00120	20	0.5	0.0061	2.00E-04	0.0235	7.62E-05	3.8525	1.27E-01	1.30E-05	4.00E-07	0.00283	2.903E-05
00121	30	0.5	0.0061	2.00E-04	0.0235	7.62E-05	3.8525	1.27E-01	1.36E-05	4.00E-07	0.00287	2.821E-05
00123	30	0.5	0.0062	2.00E-04	0.0235	7.62E-05	3.7903	1.23E-01	1.64E-05	4.00E-07	0.00306	2.495E-05
00124	40	0.5	0.0062	2.00E-04	0.0235	7.62E-05	3.7903	1.23E-01	1.32E-05	4.00E-07	0.00285	2.875E-05
00125	40	0.5	0.0061	2.00E-04	0.0235	7.62E-05	3.8525	1.27E-01	9.11E-06	4.00E-07	0.00251	3.683E-05
00126	40	0.5	0.0062	2.00E-04	0.0235	7.62E-05	3.7903	1.23E-01	1.69E-05	4.00E-07	0.00309	2.448E-05
00127	50	0.5	0.0062	2.00E-04	0.0235	7.62E-05	3.7903	1.23E-01	1.61E-05	4.00E-07	0.00304	2.524E-05
00128	50	0.5	0.0062	2.00E-04	0.0235	7.62E-05	3.7903	1.23E-01	1.28E-05	4.00E-07	0.00281	2.946E-05
00130	60	0.5	0.0061	2.00E-04	0.0235	7.62E-05	3.8525	1.27E-01	9.97E-06	4.00E-07	0.00259	3.468E-05
00131	60	0.5	0.0062	2.00E-04	0.0235	7.62E-05	3.7903	1.23E-01	1.44E-05	4.00E-07	0.00293	2.721E-05
00132	60	0.5	0.0062	2.00E-04	0.0235	7.62E-05	3.7903	1.23E-01	1.19E-05	4.00E-07	0.00275	3.086E-05
00133	20	0.5	0.0066	2.00E-04	0.0235	7.62E-05	3.5606	1.09E-01	1.40E-05	4.00E-07	0.0029	2.77E-05
00134	20	0.5	0.0065	2.00E-04	0.0235	7.62E-05	3.6154	1.12E-01	8.44E-06	4.00E-07	0.00245	3.876E-05
00135	20	0.5	0.0066	2.00E-04	0.0235	7.62E-05	3.5606	1.09E-01	1.46E-05	4.00E-07	0.00294	2.697E-05
00136	30	0.5	0.0066	2.00E-04	0.0235	7.62E-05	3.5606	1.09E-01	1.37E-05	4.00E-07	0.00288	2.808E-05
00137	30	0.5	0.0065	2.00E-04	0.0235	7.62E-05	3.6154	1.12E-01	9.88E-06	4.00E-07	0.00258	3.491E-05
00138	30	0.5	0.0066	2.00E-04	0.0235	7.62E-05	3.5606	1.09E-01	1.05E-05	4.00E-07	0.00264	3.342E-05
00139	40	0.5	0.0065	2.00E-04	0.0235	7.62E-05	3.6154	1.12E-01	1.61E-05	4.00E-07	0.00304	2.524E-05
00140	40	0.5	0.0065	2.00E-04	0.0235	7.62E-05	3.6154	1.12E-01	1.71E-05	4.00E-07	0.0031	2.43E-05
00141	40	0.5	0.0065	2.00E-04	0.0235	7.62E-05	3.6154	1.12E-01	1.19E-05	4.00E-07	0.00275	3.086E-05
00142	50	0.5	0.0066	2.00E-04	0.0235	7.62E-05	3.5606	1.09E-01	1.24E-05	4.00E-07	0.00278	3.006E-05
00143	50	0.5	0.0066	2.00E-04	0.0235	7.62E-05	3.5606	1.09E-01	1.47E-05	4.00E-07	0.00295	2.685E-05
00144	50	0.5	0.0066	2.00E-04	0.0235	7.62E-05	3.5606	1.09E-01	9.59E-06	4.00E-07	0.00256	3.56E-05
00145	60	0.5	0.0066	2.00E-04	0.0235	7.62E-05	3.5606	1.09E-01	1.45E-05	4.00E-07	0.00293	2.709E-05
00146	60	0.5	0.0066	2.00E-04	0.0235	7.62E-05	3.5606	1.09E-01	1.36E-05	4.00E-07	0.00287	2.821E-05
00147	60	0.5	0.0066	2.00E-04	0.0235	7.62E-05	3.5606	1.09E-01	1.51E-05	4.00E-07	0.00297	2.64E-05
00148	60	0.5	0.0088	2.00E-04	0.0235	7.62E-05	2.6705	6.13E-02	1.17E-05	4.00E-07	0.00273	3.12E-05
00149	60	0.5	0.0088	2.00E-04	0.0235	7.62E-05	2.6705	6.13E-02	1.59E-05	4.00E-07	0.00303	2.544E-05

00150	60	0.5	0.0088	2.00E-04	0.0235	7.62E-05	2.6705	6.13E-02	1.58E-05	4.00E-07	0.00302	2.554E-05
00151	50	0.5	0.0087	2.00E-04	0.0235	7.62E-05	2.7011	6.27E-02	1.18E-05	4.00E-07	0.00274	3.103E-05
00152	50	0.5	0.0087	2.00E-04	0.0235	7.62E-05	2.7011	6.27E-02	1.92E-05	4.00E-07	0.00322	2.25E-05
00153	50	0.5	0.0087	2.00E-04	0.0235	7.62E-05	2.7011	6.27E-02	1.75E-05	4.00E-07	0.00312	2.394E-05
00154	40	0.5	0.0088	2.00E-04	0.0235	7.62E-05	2.6705	6.13E-02	1.48E-05	4.00E-07	0.00295	2.674E-05
00155	40	0.5	0.0088	2.00E-04	0.0235	7.62E-05	2.6705	6.13E-02	1.57E-05	4.00E-07	0.00302	2.565E-05
00156	40	0.5	0.0087	2.00E-04	0.0235	7.62E-05	2.7011	6.27E-02	1.68E-05	4.00E-07	0.00308	2.457E-05
00157	30	0.5	0.0088	2.00E-04	0.0235	7.62E-05	2.6705	6.13E-02	1.77E-05	4.00E-07	0.00314	2.369E-05
00158	30	0.5	0.0088	2.00E-04	0.0235	7.62E-05	2.6705	6.13E-02	1.34E-05	4.00E-07	0.00286	2.848E-05
00159	30	0.5	0.0086	2.00E-04	0.0235	7.62E-05	2.7326	6.42E-02	2.19E-05	4.00E-07	0.00337	2.065E-05
00160	20	0.5	0.0087	2.00E-04	0.0235	7.62E-05	2.7011	6.27E-02	1.67E-05	4.00E-07	0.00308	2.466E-05
00161	20	0.5	0.0088	2.00E-04	0.0235	7.62E-05	2.6705	6.13E-02	1.58E-05	4.00E-07	0.00302	2.554E-05
00162	20	0.5	0.0088	2.00E-04	0.0235	7.62E-05	2.6705	6.13E-02	6.71E-06	4.00E-07	0.00227	4.513E-05
00163	20	0.5	0.009	2.00E-04	0.0235	7.62E-05	2.6111	5.86E-02	6.23E-06	4.00E-07	0.00222	4.741E-05
00164	20	0.5	0.009	2.00E-04	0.0235	7.62E-05	2.6111	5.86E-02	6.71E-06	4.00E-07	0.00227	4.513E-05
00165	20	0.5	0.0091	2.00E-04	0.0235	7.62E-05	2.5824	5.74E-02	5.37E-06	4.00E-07	0.00211	5.236E-05
00166	30	0.5	0.0091	2.00E-04	0.0235	7.62E-05	2.5824	5.74E-02	5.47E-06	4.00E-07	0.00212	5.174E-05
00167	30	0.5	0.0091	2.00E-04	0.0235	7.62E-05	2.5824	5.74E-02	6.04E-06	4.00E-07	0.00219	4.841E-05
00168	30	0.5	0.0091	2.00E-04	0.0235	7.62E-05	2.5824	5.74E-02	5.95E-06	4.00E-07	0.00218	4.893E-05
00169	40	0.5	0.0091	2.00E-04	0.0235	7.62E-05	2.5824	5.74E-02	4.41E-06	4.00E-07	0.00197	5.969E-05
00170	40	0.5	0.009	2.00E-04	0.0235	7.62E-05	2.6111	5.86E-02	7.29E-06	4.00E-07	0.00233	4.273E-05
00171	40	0.5	0.009	2.00E-04	0.0235	7.62E-05	2.6111	5.86E-02	6.71E-06	4.00E-07	0.00227	4.513E-05
00172	50	0.5	0.009	2.00E-04	0.0235	7.62E-05	2.6111	5.86E-02	6.23E-06	4.00E-07	0.00222	4.741E-05
00173	50	0.5	0.009	2.00E-04	0.0235	7.62E-05	2.6111	5.86E-02	6.14E-06	4.00E-07	0.0022	4.79E-05
00174	50	0.5	0.009	2.00E-04	0.0235	7.62E-05	2.6111	5.86E-02	6.62E-06	4.00E-07	0.00226	4.556E-05
00175	60	0.5	0.009	2.00E-04	0.0235	7.62E-05	2.6111	5.86E-02	8.82E-06	4.00E-07	0.00249	3.763E-05
00176	60	0.5	0.0091	2.00E-04	0.0235	7.62E-05	2.5824	5.74E-02	3.93E-06	4.00E-07	0.0019	6.444E-05
00177	60	0.5	0.009	2.00E-04	0.0235	7.62E-05	2.6111	5.86E-02	5.75E-06	4.00E-07	0.00216	5.001E-05
00311	20	0.5	0.005	2.00E-04	0.0235	7.62E-05	4.7	1.89E-01	5.92E-05	4.00E-07	0.00469	1.1E-05
00312	20	0.5	0.005	2.00E-04	0.0235	7.62E-05	4.7	1.89E-01	6.15E-05	4.00E-07	0.00475	1.076E-05
00313	30	0.5	0.005	2.00E-04	0.0235	7.62E-05	4.7	1.89E-01	5.94E-05	4.00E-07	0.0047	1.098E-05
00314	30	0.5	0.005	2.00E-04	0.0235	7.62E-05	4.7	1.89E-01	6.18E-05	4.00E-07	0.00476	1.073E-05
00315	40	0.5	0.005	2.00E-04	0.0235	7.62E-05	4.7	1.89E-01	6.08E-05	4.00E-07	0.00473	1.083E-05
00316	40	0.5	0.005	2.00E-04	0.0235	7.62E-05	4.7	1.89E-01	5.84E-05	4.00E-07	0.00467	1.109E-05
00317	50	0.5	0.005	2.00E-04	0.0235	7.62E-05	4.7	1.89E-01	5.76E-05	4.00E-07	0.00465	1.119E-05
00318	50	0.5	0.005	2.00E-04	0.0235	7.62E-05	4.7	1.89E-01	5.91E-05	4.00E-07	0.00469	1.101E-05
00319	60	0.5	0.005	2.00E-04	0.0235	7.62E-05	4.7	1.89E-01	5.96E-05	4.00E-07	0.0047	1.096E-05
00320	60	0.5	0.005	2.00E-04	0.0235	7.62E-05	4.7	1.89E-01	5.49E-05	4.00E-07	0.00458	1.151E-05
00341	20	0.5	0.0063	2.00E-04	0.0235	7.62E-05	3.7302	1.19E-01	5.78E-05	4.00E-07	0.00465	1.116E-05
00342	20	0.5	0.0063	2.00E-04	0.0235	7.62E-05	3.7302	1.19E-01	5.94E-05	4.00E-07	0.0047	1.098E-05
00343	30	0.5	0.0063	2.00E-04	0.0235	7.62E-05	3.7302	1.19E-01	5.61E-05	4.00E-07	0.00461	1.136E-05
00344	30	0.5	0.0063	2.00E-04	0.0235	7.62E-05	3.7302	1.19E-01	5.77E-05	4.00E-07	0.00465	1.117E-05
00345	40	0.5	0.0063	2.00E-04	0.0235	7.62E-05	3.7302	1.19E-01	5.63E-05	4.00E-07	0.00461	1.134E-05
00346	40	0.5	0.0063	2.00E-04	0.0235	7.62E-05	3.7302	1.19E-01	5.91E-05	4.00E-07	0.00469	1.101E-05
00347	50	0.5	0.0063	2.00E-04	0.0235	7.62E-05	3.7302	1.19E-01	5.72E-05	4.00E-07	0.00464	1.123E-05
00348	50	0.5	0.0063	2.00E-04	0.0235	7.62E-05	3.7302	1.19E-01	5.73E-05	4.00E-07	0.00464	1.122E-05
00349	60	0.5	0.0063	2.00E-04	0.0235	7.62E-05	3.7302	1.19E-01	5.64E-05	4.00E-07	0.00462	1.133E-05
00350	60	0.5	0.0063	2.00E-04	0.0235	7.62E-05	3.7302	1.19E-01	5.58E-05	4.00E-07	0.0046	1.14E-05

Data for impacts on glass (continued)

Video ID	Re	ΔRe	We	ΔWe	La	ΔLa	ε	Δε	SF	ΔSF	Num Spines
00118	2297.3	86.053	728.45	49.75	7245.2	137.247	1.05159	0.024424	18.542	0.1729	14
00119	2548.9	90.982	808.23	54.52	8038.7	114.096	1.05369	0.020675	19.702	0.1785	0
00120	2630.2	89.365	806.65	52.44	8576.1	102.533	1.05667	0.020567	20.067	0.1586	9
00121	2668.3	90.332	818.34	53.16	8700.4	100.239	1.13707	0.019973	20.236	0.1795	9
00123	2793	91.959	842.78	53.72	9256.4	91.457	1.1372	0.019548	20.783	0.1637	11
00124	2600.4	86.958	784.65	50.2	8617.9	101.747	1.30717	0.023623	19.934	0.178	9
00125	2333.7	82.856	715.73	47.04	7609.4	125.58	1.34034	0.0295	18.713	0.1726	3
00126	2820	92.693	850.91	54.22	9345.8	90.2498	1.34713	0.022425	20.9	0.1715	8
00127	2776.6	91.515	837.82	53.42	9202	92.2187	1.60638	0.027727	20.712	0.1734	3
00128	2568.6	86.183	775.05	49.63	8512.6	103.757	1.52574	0.027857	19.791	0.1845	2
00130	2405.2	84.224	737.65	48.31	7842.5	119.068	2.07463	0.04589	19.046	0.1799	3
00131	2673.7	88.803	806.76	51.53	8860.8	97.4663	2.22131	0.039606	20.26	0.1969	4
00132	2509.3	84.786	757.16	48.56	8316.1	107.777	2.08571	0.037784	19.523	0.2135	3
00133	2489.1	78.298	705.55	42.44	8781.4	98.8142	1.05329	0.01931	19.431	0.1744	8
00134	2134.9	73.05	614.47	38.18	7417.7	131.477	1.03659	0.024836	17.765	0.1669	9
00135	2522.8	79.084	715.09	42.98	8900	96.8194	1.03236	0.019732	19.584	0.1597	11
00136	2471.9	77.904	700.68	42.17	8720.8	99.8753	1.14433	0.022106	19.353	0.1645	11
00137	2249.9	74.81	647.57	39.94	7817.3	119.74	1.1444	0.023225	18.318	0.1907	0
00138	2264.9	73.613	642.01	38.93	7990.5	115.276	1.13566	0.024833	18.389	0.1641	2
00139	2648.5	83.566	762.27	46.41	9202	92.2187	1.32491	0.02518	20.148	0.1536	7
00140	2700	84.882	777.1	47.28	9381	89.7876	1.37413	0.024903	20.376	0.1592	6
00141	2393.5	77.592	688.88	42.22	8316.1	107.777	1.31801	0.026644	18.991	0.1719	0
00142	2388.5	76.063	677.03	40.84	8426.4	105.476	1.63821	0.032173	18.968	0.1839	2
00143	2528.3	79.214	716.65	43.07	8919.5	96.5025	1.63786	0.032566	19.609	0.1612	2
00144	2194.1	72.398	621.93	37.86	7740.7	121.829	1.64356	0.039261	18.051	0.1653	1
00145	2517.2	78.953	713.51	42.89	8880.5	97.1406	2.11659	0.041927	19.559	0.1766	1
00146	2466.2	77.773	699.05	42.07	8700.4	100.239	2.21005	0.043973	19.326	0.1857	3
00147	2550.1	79.735	722.84	43.42	8996.6	95.2764	2.20796	0.042584	19.708	0.1816	1
00148	1758.4	44.444	373.81	17.22	8271.1	108.747	2.20745	0.051183	15.861	0.1654	1
00149	1948.5	46.97	414.22	18.85	9165.3	92.7428	2.22967	0.046359	16.841	0.1577	2
00150	1944.5	46.908	413.39	18.81	9146.9	93.0099	2.22275	0.045821	16.822	0.1601	1
00151	1783.4	45.412	383.5	17.84	8293.7	108.258	1.73636	0.037314	15.993	0.1694	3
00152	2097.1	50.136	450.96	20.65	9752.6	85.3788	1.66538	0.030754	17.58	0.1506	3
00153	2032.2	48.995	437	20.05	9450.8	88.8966	1.70281	0.032564	17.261	0.1533	3
00154	1900.3	46.24	403.99	18.43	8938.9	96.1898	1.29885	0.026424	16.597	0.1472	2
00155	1940.6	46.847	412.55	18.78	9128.3	93.2805	1.2803	0.025913	16.802	0.1419	2
00156	2005.8	48.55	431.33	19.81	9328	90.4853	1.31365	0.025612	17.129	0.1439	5
00157	2020.1	48.14	429.46	19.49	9502.4	88.2564	1.14841	0.022775	17.2	0.1334	3
00158	1840.9	45.416	391.36	17.91	8659.4	100.982	1.15415	0.025543	16.292	0.1375	5

00159	2216.2	53.038	482.11	22.28	10188	81.1816	1.14642	0.02006	18.157	0.1392	6
00160	2002	48.487	430.5	19.78	9310.2	90.7237	1.07071	0.020916	17.11	0.1415	3
00161	1944.5	46.908	413.39	18.81	9146.9	93.0099	1.06796	0.020077	16.822	0.155	5
00162	1461.1	43.708	310.62	15.04	6873	151.38	1.07042	0.029161	14.235	0.1631	5
00163	1393.8	42.593	289.72	13.93	6705.3	158.603	1.09184	0.032018	13.848	0.1538	6
00164	1428.7	42.209	296.97	14.12	6873	151.38	1.05991	0.028478	14.05	0.1646	7
00165	1311.7	43.048	269.66	13.23	6380.3	174.378	1.07692	0.034235	13.366	0.1525	5
00166	1319.4	42.884	271.25	13.26	6418	172.414	1.17341	0.037689	13.412	0.1494	2
00167	1364.2	42.091	280.45	13.44	6635.8	161.77	1.17416	0.036643	13.676	0.1452	2
00168	1356.9	42.203	278.96	13.41	6600.5	163.42	1.18681	0.036046	13.633	0.1523	3
00169	1228.4	45.378	252.54	13.02	5975.4	197.962	1.39474	0.047265	12.864	0.164	3
00170	1468.4	41.92	305.22	14.34	7064	143.821	1.38421	0.037645	14.276	0.1573	3
00171	1428.7	42.209	296.97	14.12	6873	151.38	1.33824	0.034386	14.05	0.1786	5
00172	1393.8	42.593	289.72	13.93	6705.3	158.603	1.71895	0.053313	13.848	0.1564	3
00173	1386.6	42.689	288.23	13.9	6670.7	160.165	1.63889	0.054977	13.807	0.1407	2
00174	1421.8	42.275	295.55	14.08	6840.1	152.751	1.62733	0.048956	14.01	0.1543	2
00175	1564.9	41.763	325.29	14.97	7528.5	128.008	2.18954	0.06254	14.817	0.1496	1
00176	1182.2	47.188	243.04	12.99	5750.5	213.353	2.14286	0.084184	12.579	0.1673	1
00177	1357.1	43.144	282.1	13.76	6528.7	166.862	2.21705	0.074815	13.634	0.1601	1
00311	5238.4	210.29	1877.9	155.8	14613	71.8528	1.07843	0.011115	30.008	0.1912	19
00312	5305.7	212.97	1902	157.8	14800	72.1467	1.0694	0.011047	30.232	0.1857	17
00313	5244.3	210.53	1880	156	14629	71.8773	1.16797	0.012703	30.028	0.1759	14
00314	5314.4	213.32	1905.1	158.1	14825	72.1869	1.16635	0.012286	30.261	0.1803	13
00315	5285.4	212.16	1894.7	157.2	14744	72.0544	1.36007	0.013209	30.165	0.2113	12
00316	5214.6	209.35	1869.3	155.1	14546	71.7573	1.3219	0.013268	29.928	0.205	10
00317	5188.7	208.32	1860.1	154.4	14474	71.6587	1.57424	0.016862	29.841	0.1926	11
00318	5235.5	210.18	1876.8	155.7	14604	71.8407	1.55844	0.016613	29.998	0.1902	5
00319	5250.2	210.76	1882.1	156.2	14646	71.902	1.95148	0.023866	30.047	0.1619	6
00320	5107.7	205.1	1831	151.9	14248	71.3867	2.04167	0.022365	29.568	0.2065	5
00341	4124.3	131.88	1173.4	77.46	14496	71.6881	1.0759	0.011817	26.096	0.1756	9
00342	4162.2	133.07	1184.2	78.17	14629	71.8773	1.07692	0.012289	26.236	0.1623	19
00343	4083.2	130.58	1161.7	76.69	14352	71.5044	1.17059	0.012768	25.944	0.182	14
00344	4121.9	131.8	1172.7	77.41	14488	71.6767	1.1854	0.012931	26.087	0.1788	10
00345	4088.1	130.74	1163.1	76.78	14369	71.525	1.32773	0.014671	25.962	0.1804	13
00346	4155.1	132.85	1182.2	78.03	14604	71.8407	1.17879	0.013589	26.21	0.1611	9
00347	4109.9	131.42	1169.3	77.19	14445	71.6211	1.64626	0.018002	26.043	0.1891	4
00348	4112.3	131.5	1170	77.23	14454	71.6321	1.62812	0.017878	26.052	0.1871	10
00349	4090.5	130.81	1163.8	76.82	14377	71.5354	2.17207	0.023731	25.971	0.2082	3
00350	4075.9	130.35	1159.6	76.55	14326	71.474	2.12435	0.024283	25.917	0.1937	3

Data for impacts on tile

Video ID	θ (°)	Δθ (°)	t	Δt	z	Δz	V	ΔV	m	Δm	D	ΔD
00251	20	0.5	0.0112	2.00E-04	0.0235	7.62E-05	2.0982	3.81E-02	7.60E-06	4.00E-07	0.002366	4.15626E-05
00252	20	0.5	0.0112	2.00E-04	0.0235	7.62E-05	2.0982	3.81E-02	7.90E-06	4.00E-07	0.002397	4.05059E-05
00253	20	0.5	0.0112	2.00E-04	0.0235	7.62E-05	2.0982	3.81E-02	6.20E-06	4.00E-07	0.002211	4.75937E-05
00254	30	0.5	0.0112	2.00E-04	0.0235	7.62E-05	2.0982	3.81E-02	6.70E-06	4.00E-07	0.002269	4.51989E-05
00255	30	0.5	0.0112	2.00E-04	0.0235	7.62E-05	2.0982	3.81E-02	7.30E-06	4.00E-07	0.002335	4.26914E-05
00256	40	0.5	0.0112	2.00E-04	0.0235	7.62E-05	2.0982	3.81E-02	6.00E-06	4.00E-07	0.002187	4.86441E-05
00257	40	0.5	0.0112	2.00E-04	0.0235	7.62E-05	2.0982	3.81E-02	6.80E-06	4.00E-07	0.00228	4.47554E-05
00258	50	0.5	0.0112	2.00E-04	0.0235	7.62E-05	2.0982	3.81E-02	7.60E-06	4.00E-07	0.002366	4.15626E-05
00259	50	0.5	0.0112	2.00E-04	0.0235	7.62E-05	2.0982	3.81E-02	8.60E-06	4.00E-07	0.002466	3.82823E-05
00260	60	0.5	0.0112	2.00E-04	0.0235	7.62E-05	2.0982	3.81E-02	6.00E-06	4.00E-07	0.002187	4.86441E-05
00261	60	0.5	0.0112	2.00E-04	0.0235	7.62E-05	2.0982	3.81E-02	6.80E-06	4.00E-07	0.00228	4.47554E-05
00262	20	0.5	0.007	2.00E-04	0.0235	7.62E-05	3.3571	9.65E-02	6.40E-06	4.00E-07	0.002235	4.65983E-05
00263	20	0.5	0.007	2.00E-04	0.0235	7.62E-05	3.3571	9.65E-02	8.00E-06	4.00E-07	0.002407	4.01685E-05
00264	30	0.5	0.007	2.00E-04	0.0235	7.62E-05	3.3571	9.65E-02	8.30E-06	4.00E-07	0.002437	3.91969E-05
00265	30	0.5	0.007	2.00E-04	0.0235	7.62E-05	3.3571	9.65E-02	5.20E-06	4.00E-07	0.002085	5.35075E-05
00266	40	0.5	0.007	2.00E-04	0.0235	7.62E-05	3.3571	9.65E-02	8.30E-06	4.00E-07	0.002437	3.91969E-05
00267	40	0.5	0.007	2.00E-04	0.0235	7.62E-05	3.3571	9.65E-02	1.04E-05	4.00E-07	0.002627	3.37408E-05
00268	50	0.5	0.007	2.00E-04	0.0235	7.62E-05	3.3571	9.65E-02	8.80E-06	4.00E-07	0.002485	3.77017E-05
00269	50	0.5	0.007	2.00E-04	0.0235	7.62E-05	3.3571	9.65E-02	1.22E-05	4.00E-07	0.002771	3.03495E-05
00270	60	0.5	0.007	2.00E-04	0.0235	7.62E-05	3.3571	9.65E-02	7.20E-06	4.00E-07	0.002324	4.3085E-05
00271	60	0.5	0.007	2.00E-04	0.0235	7.62E-05	3.3571	9.65E-02	8.90E-06	4.00E-07	0.002494	3.74195E-05
00272	20	0.5	0.0052	2.00E-04	0.0235	7.62E-05	4.5192	1.74E-01	9.80E-06	4.00E-07	0.002576	3.50991E-05
00273	20	0.5	0.0052	2.00E-04	0.0235	7.62E-05	4.5192	1.74E-01	8.20E-06	4.00E-07	0.002427	3.95142E-05
00274	30	0.5	0.0052	2.00E-04	0.0235	7.62E-05	4.5192	1.74E-01	8.50E-06	4.00E-07	0.002456	3.85812E-05
00275	30	0.5	0.0052	2.00E-04	0.0235	7.62E-05	4.5192	1.74E-01	8.70E-06	4.00E-07	0.002475	3.79892E-05
00276	40	0.5	0.0052	2.00E-04	0.0235	7.62E-05	4.5192	1.74E-01	9.20E-06	4.00E-07	0.002522	3.6604E-05
00277	40	0.5	0.0053	2.00E-04	0.0235	7.62E-05	4.434	1.68E-01	6.90E-06	4.00E-07	0.002291	4.43227E-05
00278	50	0.5	0.0052	2.00E-04	0.0235	7.62E-05	4.5192	1.74E-01	9.20E-06	4.00E-07	0.002522	3.6604E-05
00279	50	0.5	0.0053	2.00E-04	0.0235	7.62E-05	4.434	1.68E-01	6.40E-06	4.00E-07	0.002235	4.65983E-05
00280	50	0.5	0.0053	2.00E-04	0.0235	7.62E-05	4.434	1.68E-01	5.80E-06	4.00E-07	0.002162	4.97546E-05
00281	60	0.5	0.0051	2.00E-04	0.0235	7.62E-05	4.6078	1.81E-01	1.01E-05	4.00E-07	0.002602	3.44031E-05
00282	60	0.5	0.0052	2.00E-04	0.0235	7.62E-05	4.5192	1.74E-01	9.00E-06	4.00E-07	0.002503	3.71427E-05
00301	20	0.5	0.005	2.00E-04	0.0235	7.62E-05	4.7	1.89E-01	6.26E-05	4.00E-07	0.004778	1.06589E-05
00302	20	0.5	0.005	2.00E-04	0.0235	7.62E-05	4.7	1.89E-01	6.33E-05	4.00E-07	0.004796	1.05901E-05
00303	30	0.5	0.005	2.00E-04	0.0235	7.62E-05	4.7	1.89E-01	5.91E-05	4.00E-07	0.00469	1.10147E-05
00304	30	0.5	0.005	2.00E-04	0.0235	7.62E-05	4.7	1.89E-01	5.71E-05	4.00E-07	0.004636	1.12422E-05
00305	40	0.5	0.005	2.00E-04	0.0235	7.62E-05	4.7	1.89E-01	5.38E-05	4.00E-07	0.004544	1.16512E-05
00306	40	0.5	0.005	2.00E-04	0.0235	7.62E-05	4.7	1.89E-01	5.37E-05	4.00E-07	0.004541	1.16643E-05
00307	50	0.5	0.005	2.00E-04	0.0235	7.62E-05	4.7	1.89E-01	5.96E-05	4.00E-07	0.004703	1.096E-05
00308	50	0.5	0.005	2.00E-04	0.0235	7.62E-05	4.7	1.89E-01	5.94E-05	4.00E-07	0.004698	1.09818E-05
00309	60	0.5	0.005	2.00E-04	0.0235	7.62E-05	4.7	1.89E-01	6.18E-05	4.00E-07	0.00476	1.07292E-05
00310	60	0.5	0.005	2.00E-04	0.0235	7.62E-05	4.7	1.89E-01	6.19E-05	4.00E-07	0.004763	1.0719E-05
00331	20	0.5	0.0063	2.00E-04	0.0235	7.62E-05	3.7302	1.19E-01	5.83E-05	4.00E-07	0.004668	1.1104E-05
00332	20	0.5	0.0063	2.00E-04	0.0235	7.62E-05	3.7302	1.19E-01	6.13E-05	4.00E-07	0.004747	1.07803E-05
00333	30	0.5	0.0063	2.00E-04	0.0235	7.62E-05	3.7302	1.19E-01	5.66E-05	4.00E-07	0.004622	1.13013E-05
00334	30	0.5	0.0063	2.00E-04	0.0235	7.62E-05	3.7302	1.19E-01	5.91E-05	4.00E-07	0.00469	1.10147E-05
00335	40	0.5	0.0063	2.00E-04	0.0235	7.62E-05	3.7302	1.19E-01	5.78E-05	4.00E-07	0.004655	1.11609E-05
00336	40	0.5	0.0063	2.00E-04	0.0235	7.62E-05	3.7302	1.19E-01	6.15E-05	4.00E-07	0.004753	1.07597E-05
00337	50	0.5	0.0063	2.00E-04	0.0235	7.62E-05	3.7302	1.19E-01	5.90E-05	4.00E-07	0.004687	1.10257E-05
00338	50	0.5	0.0063	2.00E-04	0.0235	7.62E-05	3.7302	1.19E-01	5.94E-05	4.00E-07	0.004698	1.09818E-05
00339	60	0.5	0.0063	2.00E-04	0.0235	7.62E-05	3.7302	1.19E-01	5.87E-05	4.00E-07	0.004679	1.1059E-05
00340	60	0.5	0.0063	2.00E-04	0.0235	7.62E-05	3.7302	1.19E-01	5.80E-05	4.00E-07	0.00466	1.1138E-05

Data for impacts on tile (continued)

00251	1176.52	29.7904	195.089	7.79	7095.294	140.183	1.0497	0.0382	8.6223	0.11172	6
00252	1191.81	29.6322	197.622	7.84	7187.451	136.892	1.1075	0.034	12.194	0.14064	10
00253	1099.33	31.0154	182.288	7.587	6629.739	159.181	1.0683	0.0385	10.358	0.13342	6
00254	1128.12	30.4689	187.062	7.651	6803.37	151.599	1.2216	0.0399	12.101	0.14556	6
00255	1160.84	29.9796	192.487	7.741	7000.678	143.712	1.2105	0.0388	11.874	0.14095	4
00256	1087.38	31.2771	180.306	7.564	6557.671	162.52	1.415	0.0493	11.689	0.14694	2
00257	1133.7	30.3758	187.988	7.665	6837.051	150.199	1.4118	0.0473	11.623	0.14222	3
00258	1176.52	29.7904	195.089	7.79	7095.294	140.183	1.7551	0.0562	12.385	0.14702	2
00259	1226.02	29.3644	203.295	7.963	7393.76	130.017	1.7325	0.0522	12.842	0.14634	2
00260	1087.38	31.2771	180.306	7.564	6557.671	162.52	2.4286	0.0918	11.647	0.15509	1
00261	1133.7	30.3758	187.988	7.665	6837.051	150.199	2.4153	0.0868	11.828	0.15198	1
00262	1777.64	63.2236	471.622	28.67	6700.273	156.024	1.0754	0.0313	15.595	0.17367	16
00263	1914.9	63.7563	508.039	30.29	7217.65	135.844	1.0948	0.0298	15.382	0.164	17
00264	1938.55	63.9664	514.312	30.59	7306.766	132.836	1.1667	0.0319	14.951	0.1598	16
00265	1658.76	63.999	440.083	27.46	6252.211	178.062	1.2	0.0377	15.456	0.18116	11
00266	1938.55	63.9664	514.312	30.59	7306.766	132.836	1.3498	0.0347	17.128	0.17629	10
00267	2089.91	65.9241	554.47	32.59	7877.292	116.245	1.3636	0.0322	17.486	0.17081	11
00268	1976.72	64.366	524.439	31.08	7450.637	128.234	1.701	0.0418	18.96	0.18958	5
00269	2204.13	67.9378	584.773	34.17	8307.795	106.298	1.7159	0.0463	12.661	0.13424	4
00270	1848.82	63.341	490.506	29.49	6968.565	144.946	2.3544	0.0637	19.899	0.21141	3
00271	1984.17	64.4522	526.418	31.18	7478.753	127.37	2.2588	0.0575	19.188	0.1962	3
00272	2758.16	113.009	985.066	77.08	7722.796	120.319	1.0844	0.0264	16.79	0.16693	21
00273	2599.06	108.978	928.242	73.05	7277.303	133.817	1.0789	0.0274	17.412	0.17758	21
00274	2630.37	109.714	939.427	73.83	7364.99	130.937	1.1853	0.0283	19.337	0.1899	20
00275	2650.84	110.212	946.738	74.35	7422.307	129.117	1.1617	0.0276	19.145	0.18761	21
00276	2700.68	111.473	964.538	75.61	7561.857	124.88	1.3677	0.0319	19.555	0.18934	10
00277	2407.44	102.477	843.583	65.72	6870.403	148.836	1.3596	0.0349	19.514	0.20048	8
00278	2700.68	111.473	964.538	75.61	7561.857	124.88	1.6509	0.0375	21.333	0.20353	8
00279	2347.82	101.599	822.694	64.38	6700.273	156.024	1.5707	0.0419	19.473	0.20512	4
00280	2272.03	100.77	796.137	62.72	6483.983	166.057	1.6215	0.0444	19.865	0.21282	6
00281	2840.65	118.032	1034.42	82.41	7800.809	118.226	2.1846	0.049	22.443	0.21245	1
00282	2680.97	110.966	957.497	75.11	7506.659	126.523	2.095	0.0464	24.449	0.22982	4
00301	5334.48	214.115	1912.32	158.7	14880.66	72.2824	1.0769	0.0117	25.833	0.16977	35

00302	5354.41	214.908	1919.47	159.3	14936.28	72.38	1.0631	0.0115	25.885	0.16976	42
00303	5235.45	210.175	1876.82	155.7	14604.43	71.8407	1.1809	0.013	26.192	0.17318	35
00304	5175.41	207.788	1855.3	154	14436.93	71.6101	1.1736	0.0135	24.662	0.16593	35
00305	5073.17	203.727	1818.65	150.9	14151.75	71.2886	1.3203	0.0151	26.311	0.17658	26
00306	5070.01	203.602	1817.52	150.8	14142.92	71.2802	1.3385	0.0154	25.902	0.17454	21
00307	5250.25	210.764	1882.13	156.2	14645.71	71.902	1.6405	0.0173	30.128	0.19547	8
00308	5244.34	210.529	1880.01	156	14629.22	71.8773	1.6454	0.0164	33.813	0.21452	7
00309	5314.39	213.315	1905.12	158.1	14824.63	72.1869	2.1138	0.0226	30.675	0.2004	9
00310	5317.27	213.43	1906.15	158.2	14832.66	72.2004	2.0915	0.0218	32.258	0.20839	7
00331	4136.19	132.251	1176.79	77.68	14537.89	71.7456	1.078	0.0125	23.842	0.16092	29
00332	4206.31	134.46	1196.74	78.99	14784.34	72.1201	1.0423	0.0124	21.936	0.14962	32
00333	4095.38	130.967	1165.18	76.92	14394.44	71.5564	1.1783	0.0139	23.589	0.16045	27
00334	4155.12	132.847	1182.18	78.03	14604.43	71.8407	1.1602	0.0133	24.121	0.16223	32
00335	4124.27	131.876	1173.4	77.46	14496	71.6881	1.3311	0.0153	24.629	0.16596	20
00336	4210.9	134.605	1198.05	79.08	14800.48	72.1467	1.363	0.0158	23.455	0.15841	15
00337	4152.76	132.773	1181.51	77.99	14596.14	71.8286	1.6483	0.019	25.276	0.17038	7
00338	4162.17	133.07	1184.18	78.17	14629.22	71.8773	1.6454	0.0188	25.721	0.17256	6
00339	4145.68	132.55	1179.49	77.86	14571.24	71.7927	2.1496	0.0248	27.479	0.18528	3
00340	4129.05	132.026	1174.76	77.55	14512.78	71.7109	2.1398	0.0253	26.287	0.17919	5

Data for impacts on paper

Video ID	θ (°)	Δθ (°)	t	Δt	z	Δz	V	ΔV	m	Δm	D	ΔD
00211	20	0.5	0.007	2.00E-04	0.0235	7.62E-05	3.3571	9.65E-02	4.70E-06	4.00E-07	0.002016	5.7235E-05
00212	20	0.5	0.0072	2.00E-04	0.0235	7.62E-05	3.2639	9.13E-02	3.30E-06	4.00E-07	0.001792	7.2442E-05
00213	30	0.5	0.0074	2.00E-04	0.0235	7.62E-05	3.1757	8.64E-02	2.00E-06	4.00E-07	0.001516	0.00010114
00214	30	0.5	0.0072	2.00E-04	0.0235	7.62E-05	3.2639	9.13E-02	2.80E-06	4.00E-07	0.001696	8.0825E-05
00215	40	0.5	0.007	2.00E-04	0.0235	7.62E-05	3.3571	9.65E-02	7.90E-06	4.00E-07	0.002397	4.0506E-05
00216	40	0.5	0.007	2.00E-04	0.0235	7.62E-05	3.3571	9.65E-02	2.20E-06	4.00E-07	0.001565	9.4919E-05
00217	50	0.5	0.0073	2.00E-04	0.0235	7.62E-05	3.2192	8.88E-02	2.20E-06	4.00E-07	0.001565	9.4919E-05
00218	50	0.5	0.0072	2.00E-04	0.0235	7.62E-05	3.2639	9.13E-02	3.80E-06	4.00E-07	0.001878	6.5942E-05
00219	60	0.5	0.0072	2.00E-04	0.0235	7.62E-05	3.2639	9.13E-02	4.70E-06	4.00E-07	0.002016	5.7235E-05
00220	60	0.5	0.0071	2.00E-04	0.0235	7.62E-05	3.3099	9.39E-02	4.10E-06	4.00E-07	0.001926	6.2686E-05
00221	20	0.5	0.0056	2.00E-04	0.0235	7.62E-05	4.1964	1.50E-01	2.50E-06	4.00E-07	0.001633	8.7166E-05
00222	20	0.5	0.0058	2.00E-04	0.0235	7.62E-05	4.0517	1.40E-01	1.80E-06	4.00E-07	0.001464	0.0001085
00223	30	0.5	0.0056	2.00E-04	0.0235	7.62E-05	4.1964	1.50E-01	3.20E-06	4.00E-07	0.001774	7.3943E-05
00224	30	0.5	0.0058	2.00E-04	0.0235	7.62E-05	4.0517	1.40E-01	1.40E-06	4.00E-07	0.001346	0.00012829
00225	40	0.5	0.0055	2.00E-04	0.0235	7.62E-05	4.2727	1.56E-01	4.20E-06	4.00E-07	0.001942	6.1688E-05
00226	40	0.5	0.0056	2.00E-04	0.0235	7.62E-05	4.1964	1.50E-01	3.20E-06	4.00E-07	0.001774	7.3943E-05
00227	50	0.5	0.0056	2.00E-04	0.0235	7.62E-05	4.1964	1.50E-01	2.70E-06	4.00E-07	0.001676	8.2808E-05
00228	50	0.5	0.0056	2.00E-04	0.0235	7.62E-05	4.1964	1.50E-01	2.50E-06	4.00E-07	0.001633	8.7166E-05
00229	60	0.5	0.0057	2.00E-04	0.0235	7.62E-05	4.1228	1.45E-01	2.30E-06	4.00E-07	0.001589	9.2148E-05
00230	60	0.5	0.0055	2.00E-04	0.0235	7.62E-05	4.2727	1.56E-01	5.30E-06	4.00E-07	0.002098	5.2833E-05
00283	20	0.5	0.0052	2.00E-04	0.0235	7.62E-05	4.5192	1.74E-01	8.00E-06	4.00E-07	0.002407	4.0168E-05
00284	20	0.5	0.005	2.00E-04	0.0235	7.62E-05	4.7	1.89E-01	1.28E-05	4.00E-07	0.002815	2.9399E-05
00285	30	0.5	0.0051	2.00E-04	0.0235	7.62E-05	4.6078	1.81E-01	1.02E-05	4.00E-07	0.00261	3.4179E-05
00286	30	0.5	0.0052	2.00E-04	0.0235	7.62E-05	4.5192	1.74E-01	8.50E-06	4.00E-07	0.002456	3.8581E-05
00287	30	0.5	0.0052	2.00E-04	0.0235	7.62E-05	4.5192	1.74E-01	9.20E-06	4.00E-07	0.002522	3.6604E-05
00288	30	0.5	0.0052	2.00E-04	0.0235	7.62E-05	4.5192	1.74E-01	9.00E-06	4.00E-07	0.002503	3.7143E-05
00289	40	0.5	0.0052	2.00E-04	0.0235	7.62E-05	4.5192	1.74E-01	1.06E-05	4.00E-07	0.002644	3.3317E-05
00290	40	0.5	0.0051	2.00E-04	0.0235	7.62E-05	4.6078	1.81E-01	1.02E-05	4.00E-07	0.00261	3.4179E-05
00291	50	0.5	0.0052	2.00E-04	0.0235	7.62E-05	4.5192	1.74E-01	9.90E-06	4.00E-07	0.002584	3.4863E-05
00292	50	0.5	0.0052	2.00E-04	0.0235	7.62E-05	4.5192	1.74E-01	9.20E-06	4.00E-07	0.002522	3.6604E-05
00293	60	0.5	0.0052	2.00E-04	0.0235	7.62E-05	4.5192	1.74E-01	8.90E-06	4.00E-07	0.002494	3.742E-05
00294	60	0.5	0.0052	2.00E-04	0.0235	7.62E-05	4.5192	1.74E-01	1.07E-05	4.00E-07	0.002652	3.311E-05
00321	20	0.5	0.005	2.00E-04	0.0235	7.62E-05	4.7	1.89E-01	5.79E-05	4.00E-07	0.004658	1.1149E-05
00322	20	0.5	0.005	2.00E-04	0.0235	7.62E-05	4.7	1.89E-01	5.79E-05	4.00E-07	0.004658	1.1149E-05
00323	30	0.5	0.005	2.00E-04	0.0235	7.62E-05	4.7	1.89E-01	5.74E-05	4.00E-07	0.004644	1.1207E-05
00324	30	0.5	0.005	2.00E-04	0.0235	7.62E-05	4.7	1.89E-01	5.80E-05	4.00E-07	0.00466	1.1138E-05
00325	40	0.5	0.005	2.00E-04	0.0235	7.62E-05	4.7	1.89E-01	5.67E-05	4.00E-07	0.004625	1.1289E-05
00326	40	0.5	0.005	2.00E-04	0.0235	7.62E-05	4.7	1.89E-01	5.58E-05	4.00E-07	0.0046	1.1398E-05
00327	50	0.5	0.005	2.00E-04	0.0235	7.62E-05	4.7	1.89E-01	5.34E-05	4.00E-07	0.004533	1.1704E-05
00328	50	0.5	0.005	2.00E-04	0.0235	7.62E-05	4.7	1.89E-01	5.99E-05	4.00E-07	0.004711	1.0928E-05
00329	60	0.5	0.005	2.00E-04	0.0235	7.62E-05	4.7	1.89E-01	6.07E-05	4.00E-07	0.004732	1.0843E-05
00330	60	0.5	0.005	2.00E-04	0.0235	7.62E-05	4.7	1.89E-01	5.82E-05	4.00E-07	0.004666	1.1115E-05
00351	20	0.5	0.0063	2.00E-04	0.0235	7.62E-05	3.7302	1.19E-01	5.58E-05	4.00E-07	0.0046	1.1398E-05
00352	20	0.5	0.0063	2.00E-04	0.0235	7.62E-05	3.7302	1.19E-01	5.55E-05	4.00E-07	0.004592	1.1435E-05
00353	30	0.5	0.0063	2.00E-04	0.0235	7.62E-05	3.7302	1.19E-01	5.65E-05	4.00E-07	0.004619	1.1313E-05
00354	30	0.5	0.0063	2.00E-04	0.0235	7.62E-05	3.7302	1.19E-01	5.84E-05	4.00E-07	0.004671	1.1093E-05
00355	40	0.5	0.0063	2.00E-04	0.0235	7.62E-05	3.7302	1.19E-01	5.95E-05	4.00E-07	0.0047	1.0971E-05
00356	40	0.5	0.0063	2.00E-04	0.0235	7.62E-05	3.7302	1.19E-01	5.91E-05	4.00E-07	0.00469	1.1015E-05
00357	50	0.5	0.0063	2.00E-04	0.0235	7.62E-05	3.7302	1.19E-01	5.79E-05	4.00E-07	0.004658	1.1149E-05
00358	50	0.5	0.0063	2.00E-04	0.0235	7.62E-05	3.7302	1.19E-01	5.86E-05	4.00E-07	0.004676	1.107E-05
00359	60	0.5	0.0063	2.00E-04	0.0235	7.62E-05	3.7302	1.19E-01	5.64E-05	4.00E-07	0.004617	1.1325E-05
00360	60	0.5	0.0063	2.00E-04	0.0235	7.62E-05	3.7302	1.19E-01	5.48E-05	4.00E-07	0.004572	1.1523E-05

00211	1638.746	64.8708	418.1382	26.99398	6422.488	190.047	1.17123	0.038092	11.34745	0.15192	16
00212	1416.063	68.1732	351.2823	24.19944	5708.324	239.338	1.05755	0.041991	11.7563	0.1689	13
00213	1165.973	82.2339	281.4253	23.82625	4830.744	333.129	1.30172	0.04573	14.07223	0.21542	12
00214	1340.594	72.5235	332.5607	24.28187	5404.1	266.667	1.22603	0.037308	16.77703	0.22142	11
00215	1948.444	63.6921	497.1601	30.19341	7636.242	136.892	1.41045	0.038261	8.142599	0.10932	10
00216	1272.389	83.6004	324.6595	26.7957	4986.681	312.743	1.3937	0.040571	16.94766	0.23756	6
00217	1220.099	79.5782	298.5234	24.14177	4986.681	312.743	1.70339	0.040349	17.88178	0.24966	5
00218	1484.245	65.2554	368.1964	24.35579	5983.177	218.211	1.76744	0.036414	15.4034	0.19979	4
00219	1593.225	62.2009	395.2309	24.94222	6422.488	190.047	2.91	0.040309	13.22642	0.18441	2
00220	1543.76	65.2685	388.3541	25.48454	6136.658	207.659	2.90991	0.036315	17.84915	0.23106	2
00221	1659.723	104.474	529.3634	47.19415	5203.761	287.382	1.10204	0.038927	16.42613	0.22346	11
00222	1436.282	115.019	442.3012	44.28896	4664.032	357.243	1.07801	0.041013	18.40252	0.26005	19
00223	1802.073	97.0398	574.7653	47.83489	5650.072	244.225	1.27273	0.034787	17.66064	0.22192	13
00224	1320.865	131.081	406.7585	46.96277	4289.237	422.151	1.28571	0.047619	16.37412	0.2585	12
00225	2008.926	95.2134	652.3905	52.3893	6186.15	204.428	1.45455	0.035402	14.51764	0.18461	9
00226	1802.073	97.0398	574.7653	47.83489	5650.072	244.225	1.46377	0.036591	16.31023	0.21231	12
00227	1702.852	101.791	543.1192	47.26726	5338.984	273.141	1.6383	0.034264	21.34281	0.26544	7
00228	1659.723	104.474	529.3634	47.19415	5203.761	287.382	1.97842	0.032492	26.36638	0.31627	5
00229	1585.908	105.373	496.9464	45.11141	5061.12	303.674	2.55714	0.059617	9.136828	0.17157	3
00230	2170.899	94.2993	704.9904	55.07514	6684.916	175.899	2.83636	0.036888	14.34475	0.18771	5
00283	2633.926	108.496	904.7041	72.51882	7668.328	135.844	1.15217	0.024364	19.23495	0.19142	21
00284	3203.885	130.146	1144.493	94.15974	8968.93	103.581	1.12903	0.022811	16.01943	0.15316	19
00285	2912.104	118.303	1019.866	82.65996	8315.162	117.553	1.14097	0.024799	15.77985	0.15873	14
00286	2687.695	109.714	923.1726	73.83062	7824.867	130.937	1.21393	0.02722	14.86451	0.15854	17
00287	2759.537	111.473	947.8491	75.60709	8034.027	124.88	1.22174	0.02372	18.58174	0.18191	15
00288	2739.394	110.966	940.9302	75.10649	7975.382	126.523	1.26396	0.027277	14.31137	0.15283	20
00289	2892.959	115.07	993.6769	78.96452	8422.466	114.982	1.4058	0.024802	15.75809	0.15852	12
00290	2912.104	118.303	1019.866	82.65996	8315.162	117.553	1.49756	0.024406	16.89155	0.16826	10
00291	2827.822	113.266	971.3036	77.31699	8232.828	119.608	1.715	0.023746	18.78212	0.18399	6
00292	2759.537	111.473	947.8491	75.60709	8034.027	124.88	2.1677	0.02723	16.15487	0.17233	6
00293	2729.21	110.714	937.4323	74.85413	7945.734	127.37	2.01099	0.02468	19.57957	0.19639	7
00294	2902.028	115.328	996.7919	79.19504	8448.869	114.368	2.65409	0.025977	17.4434	0.1806	3
00321	5199.591	208.749	1863.969	154.6732	14504.39	71.6994	1.09916	0.012087	21.94818	0.15101	30
00322	5199.591	208.749	1863.969	154.6732	14504.39	71.6994	1.103	0.012274	21.28784	0.14746	25
00323	5184.502	208.15	1858.56	154.2254	14462.3	71.6431	1.19134	0.01257	20.52452	0.14369	27

00324	5202.598	208.869	1865.047	154.7625	14512.78	71.7109	1.13502	0.011905	22.63815	0.15472	26
00325	5163.229	207.304	1850.934	153.594	14402.96	71.567	1.32697	0.012556	20.99747	0.14692	18
00326	5135.617	206.207	1841.036	152.7745	14325.94	71.474	1.32511	0.011803	24.01363	0.16351	19
00327	5060.497	203.224	1814.106	150.5453	14116.39	71.2554	1.65664	0.012057	24.74622	0.17008	17
00328	5259.088	211.115	1885.298	156.4393	14670.36	71.9394	1.56706	0.011563	24.59026	0.16596	14
00329	5282.514	212.047	1893.696	157.1348	14735.71	72.0414	1.95616	0.012421	22.4404	0.15626	11
00330	5208.602	209.108	1867.2	154.9407	14529.53	71.734	1.91842	0.01201	24.5352	0.16833	11
00351	4075.887	130.354	1159.634	76.55076	14325.94	71.474	1.10791	0.013688	17.55147	0.12778	28
00352	4068.529	130.122	1157.541	76.4131	14300.08	71.4442	1.09337	0.014113	16.55996	0.12232	26
00353	4092.951	130.89	1164.489	76.87007	14385.92	71.5459	1.16063	0.012635	20.48549	0.14375	19
00354	4138.565	132.326	1177.467	77.72372	14546.24	71.7573	1.19954	0.012617	20.14968	0.1413	18
00355	4164.521	133.143	1184.852	78.20953	14637.47	71.8896	1.37709	0.012359	21.09791	0.14659	16
00356	4155.12	132.847	1182.177	78.03357	14604.43	71.8407	1.3601	0.012666	20.14031	0.14148	14
00357	4126.659	131.951	1174.08	77.50089	14504.39	71.6994	1.37093	0.013003	19.39736	0.1379	8
00358	4143.309	132.475	1178.817	77.8125	14562.91	71.7808	1.65445	0.0126	21.2846	0.14917	10
00359	4090.522	130.814	1163.798	76.82461	14377.38	71.5354	2.18681	0.012011	26.20817	0.17982	9
00360	4051.258	129.579	1152.627	76.08996	14239.38	71.3774	2.17919	0.012649	24.05732	0.1689	10

References

[1] U. Buck, B. Kneubuehl, S. Nather, N. Albertini, L. Schmidt and M. Thali, "3D Bloodstain Pattern Analysis: Balistic Reconstruction of the Trajectories of Blood Drops and Determination of the Centres of Origin of the Bloodstains.," *Forensic Science International,* vol. 206, no. 1-3, pp. 22-28, 2011.

[2] P. A. Pizzola, S. Roth and P. R. D. Forest, "Blood Droplet Dynamics," *Journal of Forensic Sciences,* vol. 31, no. 1, pp. 36-49, 1986.

[3] L. Hulse-Smith and M. Illes, "A Blind Trial Evaluation of a Crime Scene Methodology for Deducing Impact Velocity and Droplet Size from Circular Bloodstains.," *Journal of Forensic Sciences,* vol. 52, no. 1, pp. 65-69, 2007.

[4] C. D. Adam, "Fundamental Studies of Bloodstain Formation and Characteristics.," *Forensic Science International,* vol. 219, no. 1-3, pp. 76-87, 2012.

[5] C. Knock and M. Davison, "Predicting the Position of the Source of Blood Stains for Angled Impacts.," *Journal of Forensic Sciences,* vol. 52, no. 5, pp. 1044-1049, 2007.

[6] "Stain Solutions," University of Illinois Extension, 2015. [Online]. Available: http://web.extension.illinois.edu/stain/staindetail.cfm?ID=5.

[7] M. Boue and M. Illes, "Robust Estimation for Area of Origin in Bloodstain Pattern Analysis via Directional Analysis," *Forensic Science International,* vol. 226, no. 1-3, pp. 223-229, 2013.

[8] J. C. Bird, S. S. Tsai and H. A. Stone, "Inclined to Splash: Triggering and Inhibiting a Splash with Tangential Velocity," *New Journal of Physics,* vol. 11, no. 6, 2009.

[9] K. Range and F. Feuillebois, "Influence of Surface Roughness on Liquid Droplet Impact," *Journal of Colloid and Interface Science,* vol. 203, pp. 16-30, 1998.

[10] "Dictionary.com," 2015. [Online]. Available: http://dictionary.reference.com/. [Accessed February 2015].

[11] A. Costello, F. Fances and F. Verdu, "Bleach interference in forensic luminol tests on porous surfaces: More about the drying time effect," *Talanta,* vol. 77, no. 4, pp. 1555-1557, 2009.

[12] B. Karger, S. Rand, T. Fracasso and H. Pfeiffer, "Bloodstain Pattern Analysis-Casework Experience.," *Forensic Science International,* vol. 181, no. 1-3, pp. 15-20, 2008.

[13] D. Attinger, C. Moore, A. Donaldson, A. Jafari and H. A. Stone, "Fluid Dynamics Topics in Bloodstain Pattern Analysis: Comparative Review and Research Opportunities.," *Forensic Science International,* vol. 231, no. 1-3, pp. 375-396, 2013.

[14] P. L. Carroll, "Results Obtained from Planar-Impact Experiment," 2010.

[15] J. Andreas, A. Hause and W. Tucker, "Boundary Tension by Pendant Drops," in *Proceedings of the Fifteenth Colloid Symposium*, Cambridge, 1938.

[16] S. Michielsen, M. Taylor, N. Parekh and F. Ji, "Bloodstain Patterns on Textile Surfaces: A Fundamental Analysis," 2012.

[17] R. Masoodi, *Modeling Imbibition of Liquids into Rigid and Swelling Porous Media,* Milwaukee: University of Wisconsin-Milwaukee, 2010.

[18] J. Kline and F. A. McClintock, "Describing Uncertainties in Single-Sample Experiments," *Mechanical Engineering,* vol. 75, 1953.